Acta Materialia 271 (2024) 119876

Contents lists available at ScienceDirect

Acta Materialia

journal homepage: www.elsevier.com/locate/actamat

In-Situ synchrotron investigation of elastic and tensile properties of oxide dispersion strengthened EUROFER97 steel for advanced fusion reactors

Tay Sparks [a], Viacheslav Kuksenko [b], Michael Gorley [b], Jan Hoffmann [c], Yu-Lung Chiu [a], Thomas Connolley [d], Michael Rieth [c], Yiqiang Wang [b,*], Biao Cai [a,*]

[a] School of Metallurgy and Materials, University of Birmingham, Birmingham, UK
[b] UK Atomic Energy Authority, Culham Science Centre, Abingdon, Oxfordshire OX14 3DB, UK
[c] Institute for Applied Materials, Karlsruhe Institute of Technology, Karlsruhe, Germany
[d] Diamond Light Source Ltd, Harwell Science and Innovation Campus, Didcot, UK

ARTICLE INFO

Keywords:
ODS ferritic steel
Elastic Properties
synchrotron x-ray diffraction
high temperature tensile testing

ABSTRACT

The augmentation of mechanical properties of reduced activation ferritic martensitic steels through the introduction of creep resistant nano-oxide particles produces a class of oxide dispersion strengthened steels, which have attracted significant interest as candidates for first wall supporting structural materials in future nuclear fusion reactors. In the present work, the effect of temperature on the elastic properties and micro-mechanics of 0.3 wt% Y_2O_3 oxide dispersion strengthened steel EUROFER97 is investigated using synchrotron high energy X-ray diffraction in-situ tensile testing at elevated temperatures, alongside the non-oxide strengthened base steel as a point of comparison. The single crystal elastic constants of both steels are experimentally determined through analysis of the diffraction peaks corresponding to specific grain families in the polycrystalline samples investigated. The effect of temperature on the evolving dislocation density and character in both materials is interrogated, providing insight into deformation mechanisms. Finally, a constitutive flow stress model is used to evaluate the factors affecting yield strength, allowing the strengthening contribution of the oxide particles to be assessed, and correlation between the thermally driven microstructural behaviour and macroscopic mechanical response to be determined.

1. Introduction

Identifying and optimising suitable candidate structural materials for use in nuclear fusion reactors is a key area of study to help realise the promise of clean, reliable fusion energy in the years to come. EUROFER97 (E97) was developed within the EU as a candidate reduced activation ferritic martensitic (RAFM) steel with stable high temperature mechanical properties. The basis of EUROFER97's design is the addition of small percentages of refractory metals (V/Ta/W) to augment high temperature mechanical properties, addition of chromium to enhance corrosion resistance, and avoidance of undesirable microalloying contents (Nb/Co/etc.) to maintain a low activation elemental composition [1–3]. As a result of these attractive characteristics, EUROFER97 was selected as the structural material for test blanket modules (TBMs) in ITER [4], and is extensively used as the structural material in DEMOnstration Fusion Power Reactor (DEMO) TBM concepts [5,6]. The limitation facing the adoption of EUROFER97 in reactor structural designs is the limited operating temperature window over which the steel maintains robust mechanical integrity, the maximum application temperature of EUROFER97 being 550 °C [7].

The operating temperature limit of EUROFER97 has been shown to be increased through control of precipitates distributed throughout the sample. These approaches have yielded two classes of advanced structural steels: castable nanostructured alloys (CNA's), and oxide dispersion strengthened (ODS) steels. The precipitates introduced in both CNA's and ODS steels are thermally stable [8,9] particles which act as dislocation/grain pins and in so doing increase mechanical strength and reduce susceptibility to thermal creep [9–11]. Precipitates utilised in CNA's are V/Ta rich MX carbides/carbonitrides; these precipitates, present even within standard RAFMs, are distributed both at grain boundaries (alongside larger $M_{23}C_6$ carbides) but also within martensite laths [12–14]. Heat treatment can be employed to enhance CNA's MX precipitate distribution.

ODS steels, meanwhile, introduce a non-native precipitate – yttrium

* Corresponding authors.
E-mail addresses: yiqiang.wang@ukaea.uk (Y. Wang), b.cai@bham.ac.uk (B. Cai).

https://doi.org/10.1016/j.actamat.2024.119876
Received 16 January 2024; Received in revised form 29 January 2024; Accepted 28 March 2024
Available online 4 April 2024

oxide nanoparticles – during fabrication most commonly by hot isostatic pressing of yttrium oxide and steel powders, producing alloys with diffuse populations of yttrium oxide nanoparticles, and small grain size [15]. The maximum application temperature of ODS EUROFER97 is at least 100 °C higher than that of EUROFER97, reported as 650 °C [16,17]. Only small Y_2O_3 concentrations are required to achieve this augmentation; additions of 0.3 wt% and 0.5 wt% are commonly used [17–20]. Both of these concentrations produce similar improvements in alloy tensile properties, although the increased strength with increasing yttria content is offset by degraded impact properties [20], and steels with higher ODS concentrations have reported significantly lower impact energy and strain to fracture at room temperature [21,22]. Indeed, whilst the introduction of ODS particles strengthen the tensile properties of the alloy, their presence causes a rise in the ductile to brittle transition temperature [15,23] and increased anisotropy in the alloy's mechanical response [24,25]. Such properties have important consequences for structural design. Therefore, it is imperative to fully understand the effects of ODS particle strengthening on alloy mechanical response under representative operating conditions. This work is on-going.

High energy synchrotron X-ray diffraction (HE-XRD) has been widely used to interrogate microstructural properties such as phase information [26] and lattice parameters [27], and in-situ tensile testing can be utilised to evaluate the crystallographic response to mechanical load – characterising lattice strain, crystallographic anisotropy, and dislocation density. When used in conjunction with other characterisation techniques such as Electron Backscatter Diffraction (EBSD) and Scanning Electron Microscopy (SEM), in-situ HE-XRD tensile testing offers the ability to determine the effect of ODS on each component of the constitutive flow model. HE-XRD analysis of similar ODS RAFM steels was successfully employed to characterise elastic properties and dislocation behaviour [28–32], but to the best of our knowledge this important analysis has not been applied to EUROFER97. Similarly constitutive flow analysis was used to investigate the relative strengthening effects governing the ultimate strengthening power of ODS [33–36], but such evaluation often relies extensively on existing literature data for elastic and dislocation properties. Together these points represent significant novelty – evaluation of the fundamental strength behaviour of a promising future structural material through in-depth characterisation of important structural properties.

In this work, HE-XRD is used in-situ to characterise the evolving microstructure of EUROFER97 and ODS EUROFER97 samples undergoing tensile testing at elevated temperature. The XRD results produced are used to characterise the single crystal elastic constants (SCECs), bulk elastic response, and elastic anisotropy of both alloys with increasing temperature. Further, differences in the evolution of dislocation density character during loading at varied temperatures are investigated by means of the modified Williamson-Hall relation. Finally, the properties investigated are used to evaluate the varying weight of individual strengthening contributions, considered through constitutive flow analysis. In this way, the work presents a comprehensive analysis of the effects of ODS particles on the EUROFER97 steel, which can inform future modelling and design decisions through determination of material elastic properties and dislocation behaviour.

2. Materials and methods

2.1. Materials and microstructure characterisation

The EUROFER97 and ODS EUROFER97 used in this research was provided by the Karlsruhe Institute of Technology in plate form. The elemental composition of each alloy is detailed in (Table 1), and a full description of the fabrication process conducted can be found for EUROFER97 in Wang et al's work [37], and for the ODS EUROFER97 in Renzetti et al's work [38].

The grain structure of both alloys was investigated using EBSD mapping applied over a 125μmx150μm area in undeformed samples at room temperature. The EBSD work employed an accelerating voltage of 20 kV, at a working distance of 15 mm, with step size 0.25 μm, and was performed using a TESCAN Mira3 Field Emission Gun Scanning Electron Microscope (SEM), with EBSD system controlled using the Oxford Instruments Aztec software. Subsequently, a second EBSD map of the undeformed ODS EUROFER97 sample was collected over a 250μmx100μm area using accelerating voltage 20 keV, working distance 15 mm, and step size 0.4 μm, in order to evaluate coarser grains, inadequately sampled in the first map. Grain analysis of all EBSD data was performed using the MTEX software [39,40], average grain size determined from the resultant grain statistics.

Table 1
Elemental composition of supplied EUROFER97 and ODS EUROFER97 plates, provided as wt%.

Alloying element	EUROFER97	ODS EUROFER97
Cr	8.95	8.92
W	1.06	1.11
Mn	0.55	0.41
V	0.202	0.193
Ta	0.12	0.08
C	0.11	0.07
Si	0.03	0.11
Mo	0.005	0.037
Y_2O_3	–	0.3

Samples for atom probe tomography (APT) examination [41,42] were prepared in the UKAEA Materials Research Facility using a FEI Helios FIB system. The 3D distribution of chemical constituents was studied using a LEAP 5000XR APT system at University of Oxford. The analyses were performed using laser pulses with a 40pJ energy and a pulse repetition rate of 100 to 200 kHz on specimens cooled to 50 K. The total analysed volume corresponded to about 30 million collected ions for the as received samples and after high-temperature tensile tests. Analysis of the APT data was performed using AP Suite 6.3.

2.2. In-situ synchrotron XRD experiments

Synchrotron two-dimensional X-ray diffraction was conducted in-situ at the I12 beamline of Diamond Light Source, Rutherford Appleton Laboratory (Oxfordshire, UK) [43] during mechanical testing of these samples in an Instron Electro-Thermal Mechanical Testing (ETMT, Fig. 1) unit at room temperature (RT), 400 °C, 550 °C, and (in the case of ODS EUROFER97) 650 °C. Tensile dog-bone samples, gauge size 7.62 × 1.52 × 0.76 mm were cut via wire electron discharge machining from the supplied alloy plates, and ground to a fine surface finish using 1200

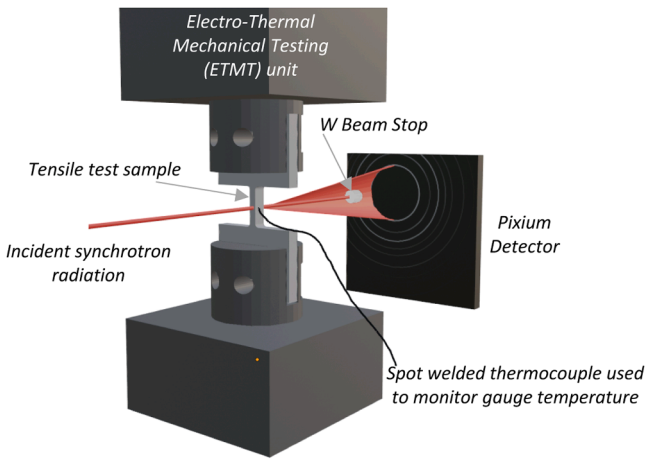

Fig. 1. Schematic representation of in-situ synchrotron XRD experimental set-up.

grit silicon carbide paper. All tests were performed in an inert atmosphere of argon, and temperature was monitored through a type R thermocouple, spot welded to the edge of each sample, with a fluctuation of test temperature over the course of testing recorded as 0.6 °C. Tensile tests were displacement controlled, with a strain rate of 0.0008 mm/s monitored using a linear variable differential transformer (LVDT). A strain gauge was not used over the experiments recorded, and so it must be noted that engineering strain quoted is a nominal value only, and may be subject to instrumental error through the effects of frame compliance, particularly at low loads. Strain rate is similarly subject to error, though over the course of the test it is expected actual strain rate should average to the reported value. Repeat load controlled tensile tests with a load rate of 1.5 N/s were conducted for selected samples: EUROFER97 at RT and 550 °C, and ODS EUROFER97 at RT. Diffraction patterns were collected using a large-area (42 × 42 cm) 2D Thales Pixium RF4343 detector with 2880 × 2881 pixel (each pixel 148 × 148 μm), each pattern requiring a capture time of 1 s. The size of the monochromatic beam was 0.5 × 0.5 mm^2, with a beam of energy 80.03 keV (wavelength 0.015 nm). The beam energy, sample-detector distance and detector tilts required for diffraction pattern analysis were determined from patterns of a CeO_2 reference sample (NIST Standard Reference Material 674b). Calibration was performed in DAWN software [44–46].

2.3. X-ray diffraction data processing

Data collected from these experiments were analysed using the DAWN Science visualisation and processing software [44–46] in conjunction with the MATLAB data analysis software for peak fitting, and the ANIZC software [47] for dislocation contrast factor determination.

2.3.1. Diffractogram peak fitting

Each 2D XRD pattern was converted to two diffractograms through integration of the pattern intensity in DAWN over two perpendicular 30° increments, one of which captured the diffracted beam in the direction of load, one the diffracted beam perpendicular to the loading direction.

Using MATLAB, a Pseudo-Voigt function was then employed to fit the diffraction peaks of each diffractogram recorded, allowing peak central position and full width half maximum to be recorded with varying macroscopic stress and strain. The Pseudo-Voigt function is a convolution of a Gaussian and Lorentzian function, and is of the form:

$$I(x) = I(0)\cdot\left[\mu\cdot e^{-\pi\frac{(x-x_0)^2}{\beta_G^2}} + (1-\mu)\cdot\frac{1}{\frac{\beta_C^2}{\pi^2}+(x-x_0)^2}\right] + h \tag{1}$$

Where $I(x)$ is the intensity, μ is the fraction of the convolution accounted for by the Gaussian model, x_0 is the peak centre, β_G and β_C are constants associated with the Gaussian and Lorentzian fits respectively, and h is the background intensity.

2.3.2. Lattice strain evolution

Having established the peak central positions for each diffraction pattern capture, grain family lattice strain was determined through observation of the shift in diffractogram peak positions over the course of deformation. The grain family strain is calculated using the equation:

$$\varepsilon_{hkl} = \frac{q_{hkl}^0}{q_{hkl}} - 1 \tag{2}$$

Where ε_{hkl} is the lattice strain experienced by the {h,k,l} indexed grain family, q_{hkl} is the diffractogram peak position (in $Å^{-1}$) under strain, and q_{hkl}^0 the diffractogram peak position prior to load being applied. Analysis of the XRD pattern produced parallel to the load direction allowed the lattice strain of the sample under tension to be determined, whilst analysis of the pattern perpendicular to load determines the evolution of lattice strain under compression.

2.3.3. Single crystal elastic constant (SCEC) calculation

The differing lattice strain-stress behaviour of individual grain families can subsequently be used to determine the material's single crystal elastic constants (SCECs). Several methods have been suggested to evaluate the SCECs in this way, but the model that most successfully accounts for orientation dependencies is the Kroner model [48], which is of the form:

$$G_{hkl}^3 - \alpha G_{hkl}^2 - \beta G_{hkl} - \gamma = 0 \tag{3}$$

Where $G_{h,k,l}$ is the diffraction modulus, and α, β, and γ are constants dependent upon the single crystal elastic constants, such that

$$\alpha = \frac{1}{5}(2\eta + 3\mu) - \frac{3}{8}(3K_M + 4(\mu + 3(\eta-\mu)A_{hkl}) \tag{4}$$

$$\beta = \frac{3}{40}(6K_M\eta + 9K_M\mu + 20\eta\mu) - \frac{3K_M}{4}(\mu + 3(\eta-\mu)A_{hkl}) \tag{5}$$

$$\gamma = \frac{3K_M\eta\mu}{4} \tag{6}$$

These equations being expressed in terms of the cubic shear moduli (μ *and* η), the bulk modulus (K_M), and the elastic anisotropy factor (A_{hkl}) defined below:

$$K_M = \frac{1}{3}(c_{11} + 2c_{12}) \tag{7}$$

$$\eta = \frac{1}{2}(c_{11} - c_{12}) \tag{8}$$

$$\mu = c_{44} \tag{9}$$

$$A_{hkl} = \frac{h^2k^2 + k^2l^2 + h^2l^2}{\left(h^2 + k^2 + l^2\right)^2} \tag{10}$$

Where c_{11}, c_{12}, and c_{44} are the material's SCECs, and h, k, and l are the principle numbers indexing the grain families considered. In conjunction with the relation in Eq. (3), the following Kroner model equations relating diffraction shear modulus to the experimentally determined diffraction elastic constants, E_{hkl}, and diffraction elastic ratios, ν_{hkl}, were used as a basis for data fitting.

$$\frac{1}{9K_M} - \frac{1}{6G_{hkl}} = -\frac{\nu_{hkl}}{E_{hkl}} \tag{11}$$

$$\frac{1}{G_{hkl}} = 2\left(\frac{1}{E_{hkl}} + \frac{\nu_{hkl}}{E_{hkl}}\right) \tag{12}$$

From these relations it was possible to evaluate the single crystal elastic constants, using MATLAB to fit the ν_{hkl}/E_{hkl}- A_{hkl} and $1/E_{hkl}$- A_{hkl} relationships.

2.3.4. Dislocation density analysis

The dislocation density was correlated to the diffractogram peak broadening through the modified Williamson-Hall (mWH) relation [49, 50], which considers the full width half maximum (FWHM) of diffractogram peaks primarily as the product of strain broadening and size effects, as shown in the Eq. (13):

$$(\Delta K)^2 \approx (0.9/D_0)^2 + \frac{\pi m^2 b^2 K^2}{2}\cdot\rho C \pm O\left(K^4C^2\right) \tag{13}$$

Where ΔK is the peak FWHM, D_0 is the average domain size, m is the effective outer radius of dislocations, K is the peak position, ρ is the dislocation density, and C is the contrast factor of the grain family. The $O(K^4C^2)$ term refers to non-interpreted higher order terms which are

considered weak relative to the size and strain terms. When modified by the contrast factor as per Eq. (13), the FWHM is therefore expected to vary linearly with peak position, with the y-intercept dependent upon particle size, and the gradient of the mWH curve directly proportional to the dislocation density. The parameter m was taken as 2, as has been successfully used in previous work [28], and the Burgers vector, b, was calculated from the lattice parameter of the alloy, further discussed in Section 3.3.

The contrast factor of dislocations with each grain family was calculated from the single crystal elastic constants previously determined, using the ANIZC software [47]. The contrast factor is dependent not only upon grain family diffraction vector, but also dislocation type, and for this reason the contrast factors relating to edge <111>{110} and screw ⟨111⟩ dislocations were calculated. The actual strain contribution should be the sum of the broadening effect of edge dislocations and screw dislocations, and so the contrast factor used should be a combination of the contrast factors calculated in proportion to their relative population, and, in fact, this allows for the dislocation character as well as total dislocation density to be approximated through the mWH plot.

3. Results and discussion

The results presented here encompass first the simple mechanical properties derived from the tensile testing of the ODS-EUROFER97/EUROFER97 samples, then the effects of temperature on the crystal lattice of the samples gathered from the diffraction data prior to load, followed by an evaluation of the elastic and microstructural changes induced by load at varying temperature, and finally examine the cumulative stress components which contribute to yield stress differences between the two materials at varying temperature.

3.1. Microstructure

The results of EBSD mapping are collected in (Fig. 2). The baseline EUROFER97 alloy exhibits an essentially untextured grain structure ([Fig. 2] c)) with an almost continuous distribution of grain sizes between 0.4–6 um, the grain size calculated via histogram being 2.14 um. The ODS EUROFER97 alloy meanwhile demonstrates significantly different microstructure. The EBSD map produced for this samples indicates a highly textured grain structure ((Fig. 2) d)), and a bimodal distribution of large and fine grains. The mapped area is dominated by fine grains with size 0.8–7.6 um, and histogram analysis produces a grain size of 1.68 um. The coarse grains (EBSD mapped in Supplementary Figure 1) primarily varied in size 7.6–20 um, though individual grains as large as 36um were observed, and a mean size of 18.32 um was found.

3.2. Tensile properties

The stress-strain curves produced during strain controlled tensile testing of the ODS-EUROFER97 and EUROFER97 samples at room temperature, 400 °C, 550 °C and 650 °C are shown in (Fig. 3) a). There is a noted difference in the mechanical response of the Y_2O_3 strengthened material at all temperatures: the ultimate tensile stress attained is significantly increased, accompanied by a reduction in the total elongation attained before fracture. The effect of temperature on the ultimate tensile strength and yield strength (determined through the 0.2 % offset method) is shown graphically in (Fig. 4). It can be noted the strengthening effect of the oxide particles is present at all test temperatures, but as temperature increases the strengthening effect is degraded, in a manner that is consistent with existing literature [35,51]. A breakdown in the effectiveness of ODS nanoparticles at elevated temperatures is also indicated by the total elongation recorded as test

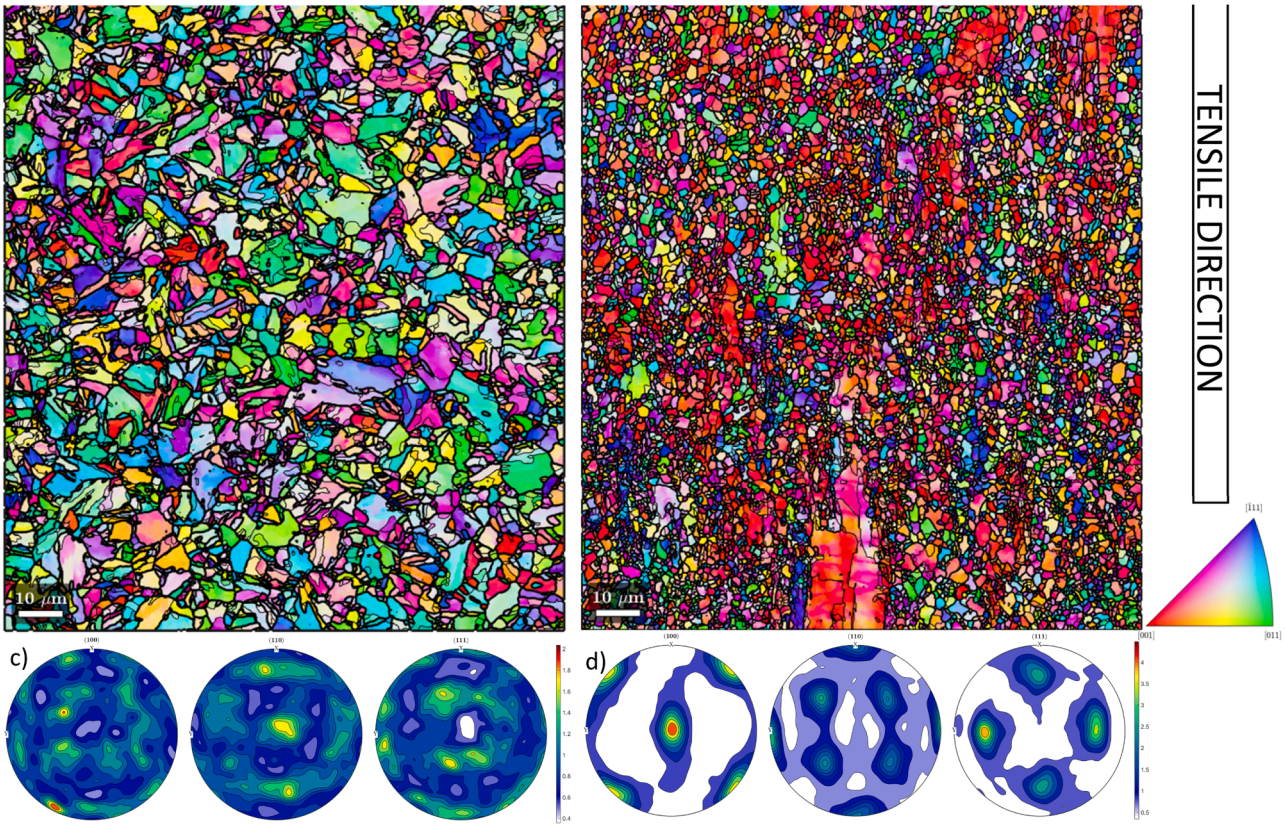

Fig. 2. EBSD map of a) EUROFER97 [and accompanying pole figure c)] and b) ODS EUROFER97 [and accompanying pole figure d)]. High angle grain boundaries (>15°) shown in bold, low angle grain boundaries (<10°) outlined lightly.

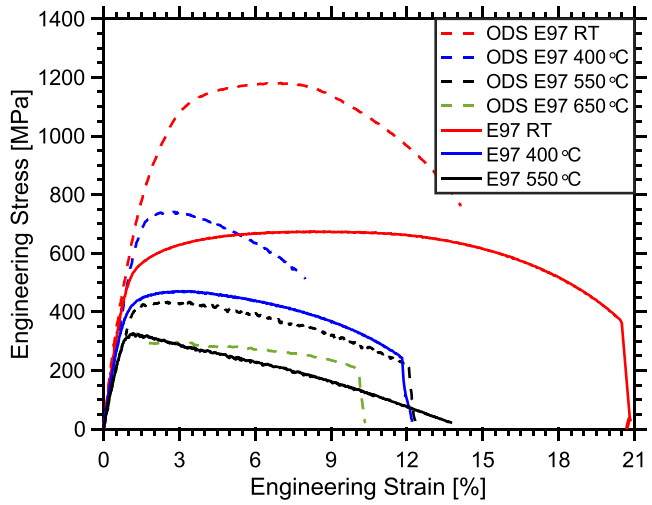

Fig. 3. Engineering stress-strain curve produced during the displacement controlled tensile testing of oxide dispersion strengthened EUROFER97 and EUROFER97 samples.

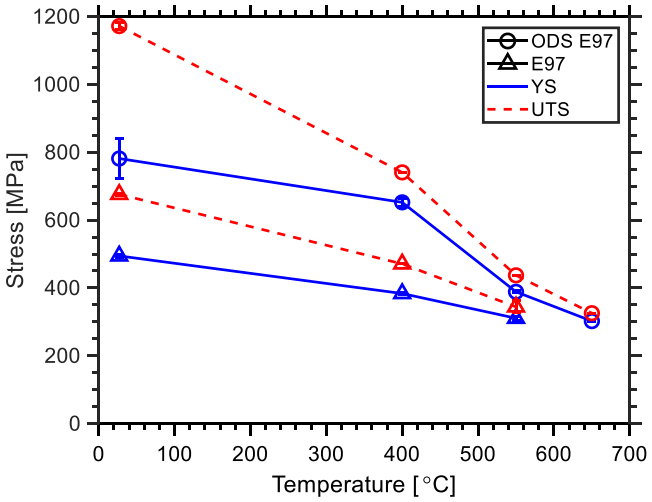

Fig. 4. Evolution of ultimate tensile stress and 0.2 % yield stress with test temperature. Data presented for EUROFER97 at RT and 550C, and ODS EUROFER97 at RT averaged over two tests (load controlled and strain controlled).

temperature was increased. Total elongation of ODS EUROFER97 samples increases as test temperature is increased from 400 °C to 550 °C, suggesting an increase in sample ductility. Furthermore, the strengthening imparted by the addition of ODS is significantly reduced at a test temperature of 550 °C (ΔYS~70 MPa) than at 400 °C (ΔYS~270 MPa). These changes can be attributed most simply to dislocations gaining energy in excess of the activation barrier corresponding to movement around such obstacles, but may also be linked to the movement agglomeration of oxide nanoparticles, into larger, less effective pinning particles. The increased total elongation observable in the 550 °C EUROFER97 curve can be linked to the curves shape during plastic deformation. After yield, there is a much more limited window of strain hardening prior to the onset of necking, and hence the sample exhibits enhanced ductility in comparison with the test performed at 400 °C.

3.3. Diffraction data analysis

Through the peak position and FWHM, XRD offers insight into microstructural deformation during macroscopic deformation. Using Bragg's law, the unloaded lattice constant of the alloy was determined from the relative position of indexed diffractogram peaks, determined at RT to be 0.28789 ± 0.0004 nm (EUROFER97) and 0.28790 ± 0.0006 nm (ODS EUROFER97). In addition to the diffraction patterns collected during tensile deformation, diffraction patterns were also collected during ramp up to target test temperature before any load was applied. As a result of this, the variation of lattice parameter with temperature, and grain family specific thermally induced lattice strain has also been recorded; associated curves can be found in Supplementary Fig. 2. The low thermal expansion coefficient of EUROFER97 is recognised as one of the attractive properties of the material, low thermal expansion promoting an enhanced thermal stress parameter. The thermal stress parameter describes the ability of a material to withstand and alleviate thermal stress without fracture, larger parameter values suggesting more effective reduction in thermal stress [52,53]. As thermal stress can be expected during heating and cooling, the ability of materials to effectively withstand thermal stress is an important performance indicator for reactor applications. Thermal stress resistance is not a purely material dependant issue – environment and specimen geometry/joining playing important roles [52] – but this parameter provides a useful point of comparison between candidate materials.

Through analysis of the curves produced for each alloy the thermal expansion coefficient at 400 °C of each alloy was determined to be $13.9 \pm 0.2 \times 10^{-6}K^{-1}$ (EUROFER97) and $12.8 \pm 0.1 \times 10^{-6}$ K^{-1} (ODS EUROFER97). These results compare well to previously literature results of 12.7×10^{-6} K^{-1} (EUROFER97 [54]) and 11.9×10^{-6} K^{-1} (ODS EUROFER97 [55]). The lowered thermal expansion coefficient, increased yield strength, and slightly reduced high temperature elastic modulus (see Section 3.3.2) suggest the ODS EUROFER97 exhibits an increased resistance to thermal stress.

3.3.1. Lattice strain evolution

Examples of the results produced by lattice strain analysis are shown in (Fig. 5 (a) and (b)), for the EUROFER97 and ODS EUROFER97 samples respectively at room temperature, with the rest of the results at high temperatures collected in Supplementary Fig. 3. From these figures, the diffraction elastic constant of each grain family (the gradient of the tensile lattice strain-stress curve prior to yield) and the diffraction elastic ratio of each grain family (the ratio between grain family curve gradients under tension and compression) can be measured. These results are collected in (Table 2).

For both alloy compositions and across all temperatures, the {222} plane was the stiffest, whilst the {200} plane was the most compliant. This distinct variation of elastic compliance with grain family orientation reveals a notable anisotropy in the alloy's mechanical responses. This anisotropy causes load partitioning within the polycrystalline sample as the sample passes the limit of elasticity and grains begin to deform plastically as differently oriented grain family's undergo micro-yielding.

Fig. 5 (c) and (d) illustrate the deviation of each grain family's response from the initial linear elastic deformation to better demonstrate the differing points of yield between differing grain families, and Supplementary Fig. 4 illustrates the nonlinear relation between engineering strain and lattice strain above low engineering strains. The compliant {200} oriented grains yield first, and the stress is redistributed about the polycrystal, increasing load experienced by the non-yielded grains. It can be observed through the increasing difference between most and least compliant grain families at higher test temperatures (for the ODS EUROFER97 samples for example: $\Delta E^{RT}_{200-222} = 68.4$ GPa, $\Delta E^{650}_{200-222} = 86.8$ GPa), that mechanical anisotropy is accentuated at higher temperature.

3.3.2. Single crystal elastic constant (SCEC)

The elasticity tensor describes the variation of a material's elastic response with orientation, information which has significant

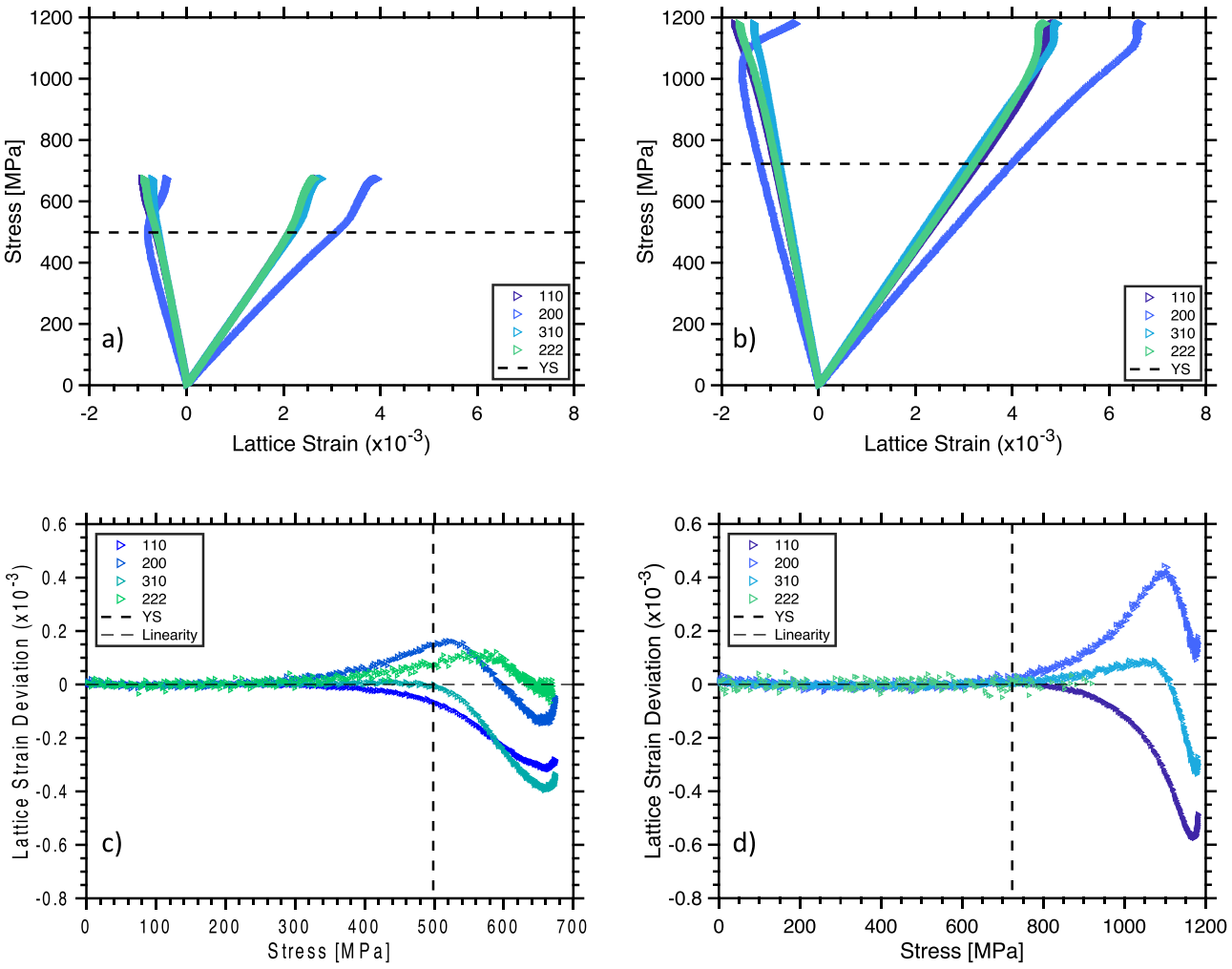

Fig. 5. Graphs demonstrating lattice strain evolution for a)/c) RT EUROFER97, and b)/d) RT ODS EUROFER97. Figures a) and b) depicting lattice strain-stress relation, figures c) and d) depicting the deviation of each grain family lattice strain-stress curve from linearity.

Table 2
Diffraction elastic constants and diffraction elastic ratio determined from lattice strain stress curves for EUROFER97 and ODS EUROFER97 samples.

Sample	Diffraction Elastic Constants [GPa]				Diffraction Elastic Ratio			
	{110}	{200}	{310}	{222}	{110}	{200}	{310}	{222}
E97 RT	228	167.0	191.9	251	0.299	0.283	0.298	0.249
	±2	±0.9	±0.8	±1	±0.001	±0.002	±0.002	±0.002
E97 400 °C	194	132.9	152.5	212	0.349	0.279	0.302	0.261
	±3	±0.9	±0.7	±1	±0.003	±0.004	±0.003	±0.003
E97 550 °C	176	106.6	126.1	184	0.350	0.307	0.327	0.244
	±3	±0.9	±0.8	±2	±0.005	±0.004	±0.003	±0.004
ODS E97 RT	220	182.6	198.9	253.2	0.3010	0.3093	0.3143	0.253
	±1	±0.7	±0.5	±0.6	±0.0005	±0.0009	±0.0007	±0.001
ODS E97 400 °C	157	128.8	139.7	204	0.30	0.35	0.341	0.30
	±2	±0.7	±0.5	±1	±0.03	±0.01	±0.006	±0.01
ODS E97 550 °C	142	99.1	113.7	186	0.262	0.316	0.315	0.22
	±2	±0.6	±0.5	±1	±0.007	±0.006	±0.006	±0.01
ODS E97 650 °C	134	95.4	106.7	182	0.161	0.35	0.31	0.14
	±2	±0.8	±0.6	±2	±0.007	±0.01	±0.01	±0.01

implications in mechanical modelling. Though the elasticity tensor has 36 components, cubic crystal symmetry allows the tensor to be reduced to only three unique components known as the single crystal elastic constants (SCECs). Despite the importance of the material information the SCECs represent, the characterisation of these properties is experimentally difficult. Historically, characterisation has been performed using ultrasonic pulsing, dependent upon the costly fabrication of large scale single crystal samples [56–58]. In this work, such difficulties are avoided - using the Kroner model fitting detailed in the method section and the plane dependant elastic properties collected in (Table 2) allow the single crystal elastic constants of the alloy to be determined directly from the polycrystalline sample.

An example of the Kroner model fits produced is shown in (Fig. 6) and the fits for each test are collected in Supplementary Fig. 5, with the

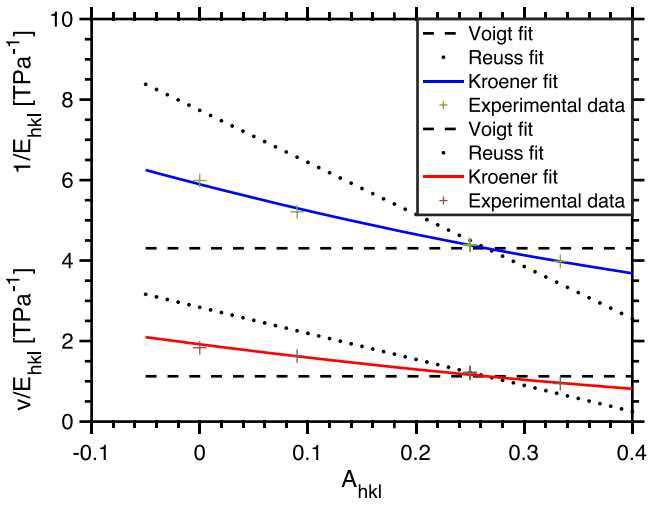

Fig. 6. Example figure (data taken for RT EUROFER97) demonstrating variation of diffraction elastic constants and ratio as a function of anisotropy, and accompanying Kroner model fit, used to determine single crystal elastic constants.

accompanying single crystal elastic constants collected in Table 3. The error associated with these values was calculated by observing the deviation of each value when the fitting was performed over ten thousand arrays, for which the diffraction elastic constant (DEC) and diffraction elastic ratio were randomised within their respective error bars.

Further, an approximation of the polycrystalline elastic properties was then determined from the single crystal elastic constants – taking a representative A_{hkl} value of 0.2 in the relations above. These results are presented alongside the single crystal elastic constants in (Table 3).

Whilst comparable experimental data is not currently available for the determination of EUROFER97 or ODS EUROFER97's SCECs, some comparison may be made with the results of experimental analysis of other similarly constituted RAFMs, and modelling based investigation. It is noted the SCEC produced for EUROFER97 at RT are appreciably similar to those experimentally determined for ferrite through ultrasonic pulse analysis of iron single crystals: C_{11}=226–233.1 GPa, C_{12}=132–140 GPa, C_{44}=115.9–117.8 GPa [58,59]. In-situ synchrotron analysis to determine SCECs has previously been applied to nanostructured ferritic alloys with similar nominal compositions as ODS EUROFER97, the most similar alloy explored being 9YWTV [Fe-9Cr-2W-0.4Ti-0.2V-0.05C-0.3Y_2O_3 (wt%)]. Gan et al.'s elastic analysis of the 9YWTV alloy produced SCEC values C_{11}=213 GPa, C_{12}=109 GPa, and C_{44}=119 GPa at RT [31]. It may be expected that there should be only minor difference between these literature values and the results presented here, given the limited difference in elemental composition and similar lattice structure. The C_{11} values recorded differ by approximately 8 %, whilst the C_{44} differ by less than 5 %. While the C_{12} value difference is proportionally more significant, the tetragonal shear modulus ($C^{'} = 0.5(C_{11} - C_{12})$) again differs by less than 10 %.

Meanwhile, theoretical modelling can provide a baseline for comparison with the EUROFER97 SCEC values produced. In their 2018 work, Li et al. numerically evaluated the SCECs of EUROFER97 at 0 K such that C_{11}=285.2 GPa, C_{12}=125.9 GPa, and C_{44}=120.3 GPa. These results are consistent with the values reported in (Table 3), the larger difference in C_{11} between modelled 0 K and experimental RT than C_{12} and C_{44} consistent with the greater induced change in C_{11} with temperature (ie that $\frac{\partial C_{11}}{\partial T} > \frac{\partial C_{12/44}}{\partial T}$).

From a bulk perspective, the results presented are in good agreement with established literature, the elastic modulus of EUROFER97 having been previously reported between 187 and 200 GPa from fatigue testing at room temperature [60], and that of ODS EUROFER97 having been reported at 212 GPa at room temperature [55]. Furthermore, characterisation of the alloys' SCECs and accompanying polycrystalline moduli, also allows for the anisotropy of the mechanical response to be evaluated, both through the Zener cubic anisotropy and by the construction of three dimensional surfaces of the elastic modulus. The Zener cubic anisotropy is calculated through the equation:

$$Z = \frac{2C_{44}}{(C_{11} - C_{12})} \tag{14}$$

And the results of this analysis are found in (Table 3). The elastic modulus surfaces with varying temperature for both alloys are illustrated in (Fig. 7). As was inferred from the increasing variance between diffraction elastic constants with increasing temperature, both alloys experience increased anisotropy at high temperature, demonstrated by the increasing Zener anisotropy, and sharpened contours of the elastic modulus surface. An increase in Zener anisotropy is expected as the temperature approaches the Curie temperature – as the tetragonal shear modulus rapidly decreases [61], while the trigonal shear modulus (C_{44}) remains relatively stable. The Curie temperature of EUROFER97 has been previously determined as 752–757 °C [62,63], while that of ODS EUROFER97 has been measured at 747 °C [33]. The relation between tetragonal shear modulus and temperature has previously been described [29] through the fit

$$C^{'} = a\sqrt{(1 - T/Tc)} \tag{15}$$

Where a is a material dependent parameter, and T_C is the Curie temperature. From this relation T_c can be determined by plotting $(C')^2$ against temperature, and these plots for EUROFER97 and ODS EUROFER97 are shown in Supplementary Fig. 6. Analysis of these curves produced T_C values of 770 °C and 730 °C for EUROFER97 and ODS EUROFER97 respectively, which – whilst severely limited by the number of data points available for analysis – agrees with the literature values quoted, considering the error found (±100 °C).

3.3.3. Dislocation density evolution

An example of the peak broadening seen over the course of tensile testing is shown in Supplementary Fig. 10, which was used for dislocation characterisation as described in the Materials and Methods. Given the known expected linear relationship described in Equation ((13), we can use the goodness of fit parameter R^2 as an indicator of the correctness of edge/screw proportion used [64]. The closer R^2 becomes to one, the more accurate the edge/screw proportion used may be considered

Table 3
Single crystal elastic constants and polycrystalline moduli determined from Kroner model fitting.

Sample	C_{11} [GPa]	C_{12} [GPa]	C_{44} [GPa]	Zener Anisotropy	Elastic Modulus [GPa]	Shear Modulus [GPa]	Poisson's Ratio
E97 RT	230±10	130±10	119±1	2.5 ± 0.3	213.6 ± 0.8	83.2 ± 0.8	0.28±0.02
E97 400 °C	207±9	140±10	122±1	3.0 ± 0.6	174.0 ± 0.6	66.5 ± 0.3	0.296±0.004
E97 550 °C	170±10	120±10	109±3	4 ± 1	161±1	62±1	0.30±0.01
ODS E97 RT	243±5	136±6	114.0 ± 0.6	2.1 ± 0.1	217.9 ± 0.4	84.6 ± 0.4	0.27±0.01
ODS E97 400 °C	192±5	128±5	93.8 ± 0.5	2.9 ± 0.4	163.2 ± 0.4	61.9 ± 0.3	0.318±0.007
ODS E97 550 °C	126±4	81±4	100±1	4.4 ± 0.6	141.3 ± 0.4	56.3 ± 0.4	0.32±0.01
ODS E97 650 °C	102±4	59±5	107±2	5.0 ± 0.7	136.2 ± 0.6	57.1 ± 0.9	0.19±0.02

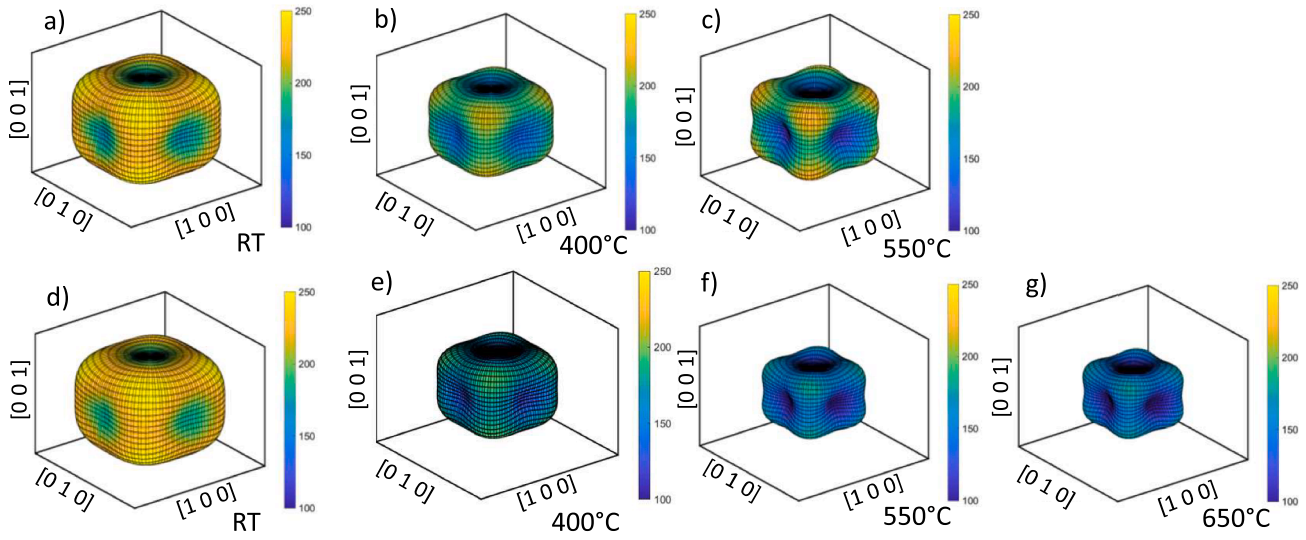

Fig. 7. Three dimensional variation of polycrystalline elastic modulus for EUROFER97 (a)-c)) and ODS EUROFER97 (d)-g)) across test temperatures. Test temperature considered indicated on each subfigure.

[65]. An example of this is illustrated in (Fig. 8), in which the data for unstrained ODS EUROFER97 at RT is used. When either purely edge (Fig. 8 (a)) or purely screw (Fig. 8 (b)) dislocation populations were considered, the data did not produce a convincing linear fit. However, when a contrast factor produced by a dislocation population 34 % Edge and 66 % Screw was used (Fig. 8 (c)), the data produced a more convincing linear fit, with a high R^2 value (0.99).

In this way, both the total dislocation density, and the dislocation density of edge and screw dislocations were estimated. The evolution of dislocation density and character with strain at varying temperature for both EUROFER97 and ODS EUROFER97 are collected in (Figs. 9 and 10), Supplementary Figs. 7–9, and tabulated in (Table 4). The dislocation density evolution in (Fig. 9) can be broadly divided into four distinct stages for each test as shown in (Fig. 9 (d)/(e)).

- Stage I: Initial constant dislocation density, corresponding to the purely elastic region of deformation.
- Stage II: Sharp increase in dislocation density at the onset of plastic deformation.
- Stage III: Increase in net dislocation density slows and then plateaus.
- Stage IV: Dislocation density falls prior to sample failure at the onset of fracture.

It is immediately apparent comparing curves of the same temperature in (Fig. 9)) that the presence of strengthening oxide particles greatly increases the maximal dislocation density reached at each test temperature. The total dislocation density-strain curves can be seen in Supplementary Figs. 7–8, and from these curves the rate of dislocation density increase during Stage II was determined from the curve between the limit of linearity and the 0.2 % offset yield stress. The rate of dislocation density produced by the ODS EUROFER97 sample was consistently greater than that of EUROFER97. This increased production of dislocations is attributed to the greater concentration of grain boundaries and material inclusions (i.e. the ODS nanoparticles) which are expected to act as dislocation sources. Neither sample presented significant temperature rate dependency.

Stage II commences prior to the macro-yield point, conventionally thought of as the transition point from elastic to plastic deformation in line with the micro-yielding behaviour observed in (Fig. 5). It is noted that the diffraction peaks started to broaden before macro-yielding (Supplementary Fig. 10). The only feasible reason for this is the multiplication of dislocations. There is a sharp increase of dislocation density across Stage II in the dislocation density verse strain curves (Fig. 9a). This is mainly because that the stress level also increases rapidly as the strain is increased during this same period. The dislocation density was then plotted against stress up to the UTS (Fig. 9), which shows that the rate of dislocation multiplication verse stress at Stage II started at a low rate then increases to be the same rate as that of the stage III.

The increase in dislocation density below macroscopic yield is the result of plastic deformation on the scale of individual grains. Dislocations are generated from grain boundaries because of orientation driven stress concentrations and move across grains to pile-up at grain boundaries: individual grains seeing plastic deformation dependent upon orientation, driving up the dislocation density. Such “micro-plastic” behaviour in polycrystalline samples has previously been observed using a variety of experimental techniques, including acoustic emission during tensile deformation [66], comparison of chemically etched deformed samples [67], in-situ TEM observation during tensile deformation [68] or loading/unloading in a sub-macro-yield regime [69], and in-situ high-energy XRD of other materials (aluminium [70,71], nickel [72], etc.).

The evolving dislocation character (edge and screw) in the ODS EUROFER97 sample with strain across all test temperatures is depicted in (Fig. 10). Dislocation density is dominated by edge type dislocations at room temperature and 400 °C (Fig. 10 (a) and (b)), moving through a mixed dislocation domain at 550 °C (Fig. 10 (c)), to a screw dominated dislocation density at 650 °C (Fig. 10 (d)). Other works reporting variable temperature tensile testing of high chromium steels have found the same dislocation character response as reported here – namely edge dominated deformation under room temperature [27,64,73], and screw dominance at >600 °C [64,65].

It is well known that BCC materials exhibit flow stress with a strong thermal dependency because of the thermally activated nature of screw dislocations. At low temperatures, the velocity of screw dislocations is significantly lower than that of edge dislocations, and so the movement of screw dislocations act as a rate determining step for the plastic deformation of BCC materials [74]. However, the temperature corresponding to thermal activation of screw dislocations is approximately 0.1 T_m, and has recently been compellingly linked to the DBTT [75–77]. All tests performed in this work were well above the DBTT of EUROFER97 and ODS EUROFER97, meaning screw dislocations should already be fully activated. Investigation of pure BCC metals around the DBTT has found that the velocity of edge and screw dislocations becomes approximately equal above the brittle to ductile transition [75,

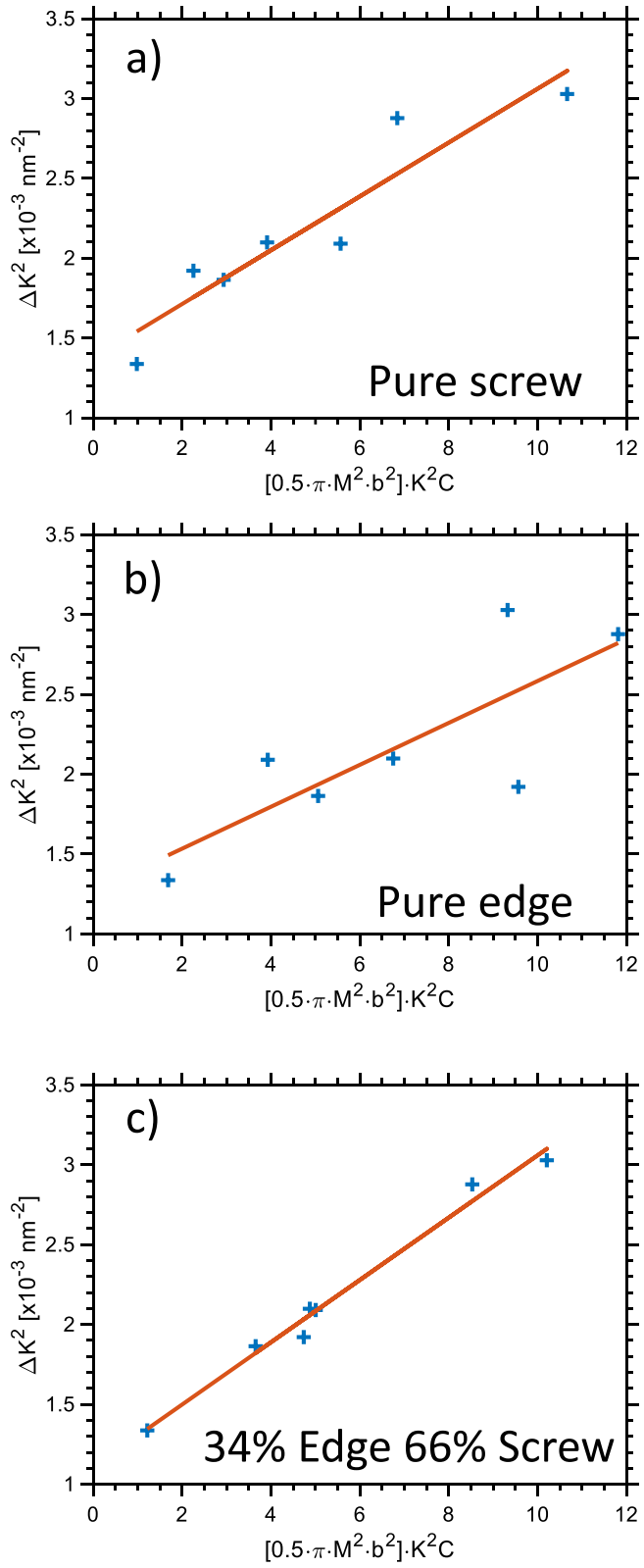

Fig. 8. Modified Williamson-Hall plots (data taken from unstrained RT ODS EUROFER97) using varying contrast factors, as dictated by the dislocation type considered, demonstrating the use of goodness of fit as a means of evaluating dislocation character. Whilst a) the pure screw case, and b) the pure edge case, produce poor linear fits, the mixed population selected in c) produces an R2 value of 0.99, an excellent linear fit.

76].

These results were determined for pure metals however, and it should be expected that alloying content will have a significant impact on dislocation behaviour. Study of BCC high entropy alloys has shown a transition from screw to edge governed plasticity as a result of the misfit between parent element and alloying content reducing the mobility of edge dislocations below that of screw dislocations [78]. This behaviour has been predicted in alloys with alloying content as low as 9.3 wt%, comparable to the total alloying content of the samples used in this work [79]. Also, to be considered is the presence of precipitates; MX/$M_{23}C_6$ carbides in EUROFER97 and Y_2O_3 nanoparticles for ODS EUROFER97. Edge dislocations in BCC metals are plane limited, whereas the ½<111> screw dislocation can glide across multiple slip planes [74], and molecular dynamics simulations have reported that precipitates within iron form stronger obstacles to edge dislocations than screw dislocations [80]. This again suggests a structure in which mobility of edge dislocations is lowered relative to that of screw dislocations, leaving the movement of edge dislocations a rate determining factor in overall plasticity. It should further be considered that the dislocation evaluation, presented in (Fig. 10) and Supplementary Fig. 9, plots how dislocation character changes, rather than actual populations of pure edge and screw dislocations. Bowing out of screw dislocations pinned at precipitates at moderate temperatures leads to highly curved dislocation segments which lowers overall screw dislocation character, as straight screw segments develop a non-screw character during curvature [81]. These factors suggest a dislocation structure at low temperature dominated by lowered mobility edge dislocations, pinned by precipitates and slowed by unusual stress valleys in the alloying content disrupted lattice.

The transition in dislocation character at elevated temperature reflects the thermally activated nature of the edge dislocation climb in body centred cubic materials [82]. At high temperature, edge dislocations gain sufficient energy to climb around precipitates, rather than bow around. Consequently, mobility of edge dislocations increases relative to that of screw dislocations, the equilibrium density of edge dislocations falls, and screw dislocations become dominant. This is borne out by the fact the equilibrium screw dislocation density remains roughly consistent across all test temperatures – ~1×10^{14} m^{-2} in the case of EUROFER97, and ~2×10^{14} m^{-2} in the case of ODS EUROFER97. Interestingly, the introduction of ODS has led to an increase in the edge dominated to screw dominated transition temperature – EUROFER97 showing a reduction in edge fraction at 400 °C, whilst ODS EUROFER97 shows a reduction in edge fraction only at 550 °C.

3.3.4. Atom probe tomography

Atom-probe tomography (APT) has been used to characterise ODS particles before and after high-temperature tensile tests. Fig. 11 shows APT investigated volumes with Y-O rich nanoclusters in the Eurofer ODS steels. The oxide particles were also enriched in V and Ti. The mean diameter of the clusters was between 3 and 10 nm and their number density were about 3.2×10^{23} m^{-3}. Eurofer ODS steel was previously investigated and detailed microstructural data can be found in works [8, 83]. Our APT experiment results are in good agreement with the previously reported data. Considering the data scatter caused by a possible inhomogeneous distribution of oxide particles, our observations suggest that there was no significant change in particle number density during the high temperature tensile tests at 400 and 550 °C. This implies that neither particle dissolution nor precipitation took place during relatively short-term thermal exposure.

3.3.5. Constitutive flow analysis

Using the physical parameters established through the XRD analysis detailed above, it is possible to evaluate the yield stress of both materials at varying temperature by considering individual strengthening contributions. The yield stress is given in this way by the relation:

$$\sigma_y = \sigma_{SS} + \sigma_{HP} + \sigma_{CC} + \sigma_d \quad (16)$$

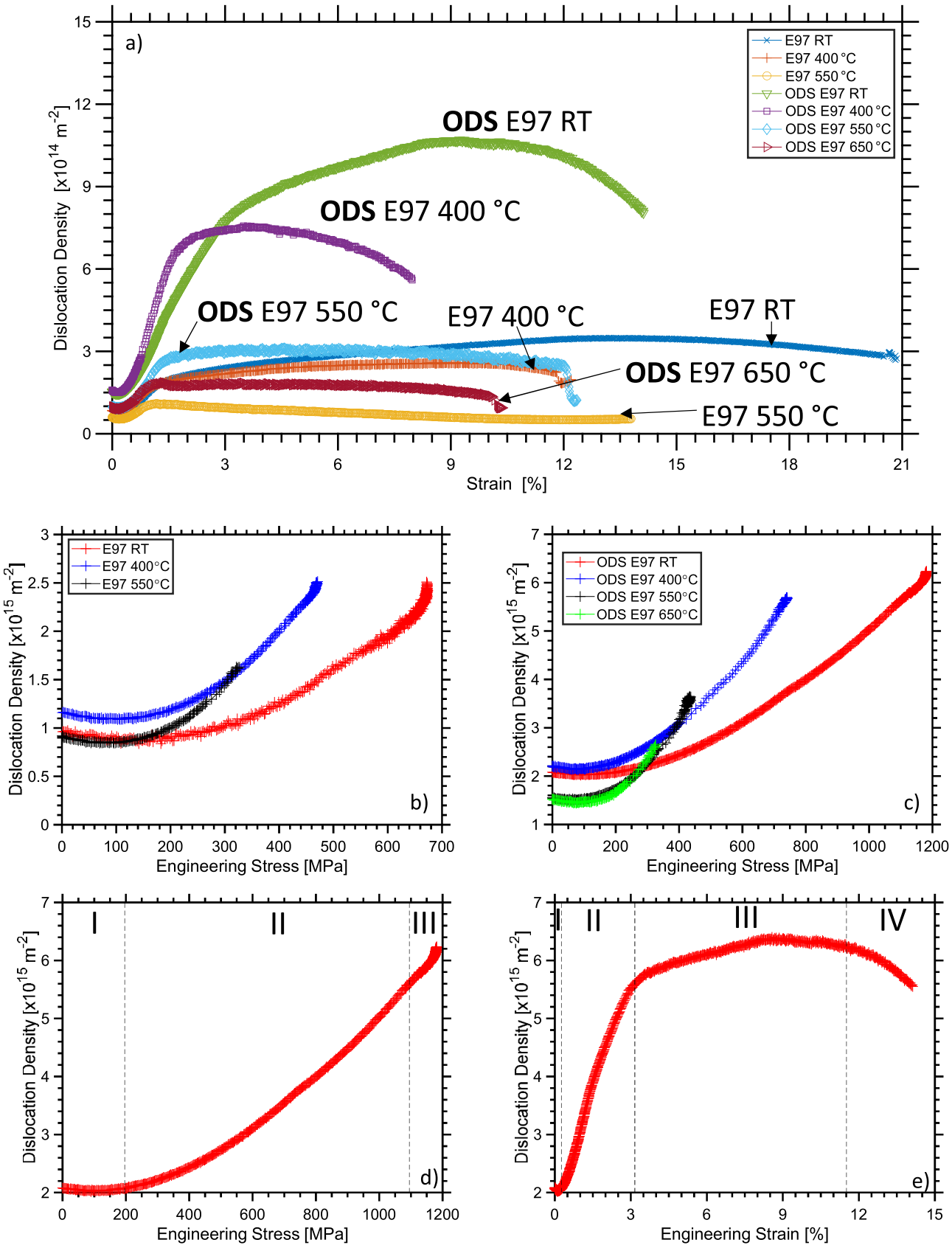

Fig. 9. Dislocation density evolution during tensile testing of EUROFER97 and ODS EUROFER97 between room temperature and 650 °C with a) engineering strain and b/c) engineering stress. Stages of dislocation density evolution are indicated on d/e) example data shown for room temperature deformation of ODS EUROFER97, transition points between stages marked by dashed lines.

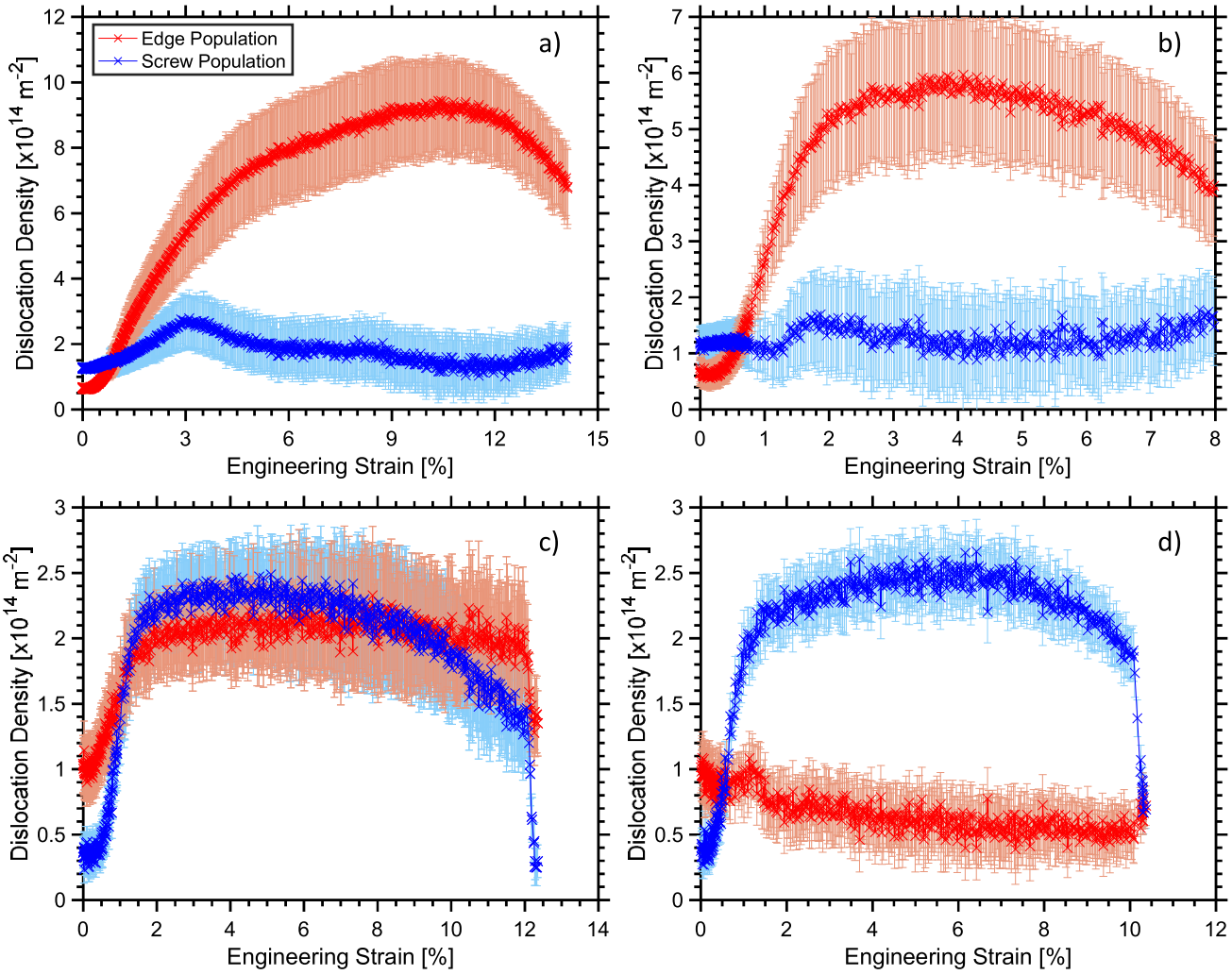

Fig. 10. Dislocation density evolution of screw (blue) and edge (red) type dislocations with strain during tensile testing of ODS EUROFER97 at RT (a), 400 °C (b), 550 °C (c), and 650 °C (d), showing the increasing screw population proportion with increasing temperature.

Table 4
Tabulated dislocation density measurements determined through the Modified Williamson Hall Method, prior to load, at the limit of linearity, and at ultimate tensile stress.

Sample		Initial dislocation density [$\times 10^{14}\, m^{-2}$]			Dislocation density at limit of linearity [$\times 10^{14}\, m^{-2}$]			Dislocation density at UTS [$\times 10^{14}\, m^{-2}$]		
		Total	Edge	Screw	Total	Edge	Screw	Total	Edge	Screw
EUROFER97	RT	0.8 ± 0.2	0.6 ± 0.2	0.3 ± 0.1	0.9 ± 0.3	0.4 ± 0.2	0.5 ± 0.2	3.1 ± 0.8	2.3 ± 0.6	0.8 ± 0.3
	400 °C	0.9 ± 0.3	0.5 ± 0.2	0.4 ± 0.2	1.0 ± 0.3	0.5 ± 0.2	0.2 ± 0.4	2.5 ± 0.6	1.2 ± 0.2	1.3 ± 0.2
	550 °C	0.7 ± 0.2	0.5 ± 0.1	0.20±0.09	0.9 ± 0.3	0.7 ± 0.2	0.2 ± 0.1	1.8 ± 0.7	1.2 ± 0.4	0.6 ± 0.3
ODS EUROFER97	RT	2.0 ± 0.7	0.8 ± 0.3	1.2 ± 0.5	1.9 ± 0.2	0.7 ± 0.1	1.3 ± 0.1	10±3	8 ± 2	2.0 ± 0.9
	400 °C	1.8 ± 0.6	0.6 ± 0.2	1.2 ± 0.2	3.1 ± 0.1	2.3 ± 0.4	1.0 ± 0.3	7 ± 2	5.5 ± 0.5	1.3 ± 0.5
	550 °C	1.4 ± 0.5	1.0 ± 0.4	0.4 ± 0.2	1.7 ± 0.6	1.2 ± 0.5	0.4 ± 0.2	4.3 ± 0.1	1.9 ± 0.3	2.4 ± 0.3
	650 °C	1.4 ± 0.5	1.0 ± 0.4	0.4 ± 0.2	1.5 ± 0.5	0.9 ± 0.3	0.6 ± 0.2	3.0 ± 0.1	0.9 ± 0.2	2.0 ± 0.2

Where σ_y is the calculated yield stress, σ_{SS} is the solid solution strengthening contribution, σ_{HP} is the Hall-Petch contribution [84,85], σ_{CC} is the Coble creep contribution [86], and σ_d is the dislocation strengthening contribution. Of these, the solid solution strengthening contribution concerns the effect of alloying element content in disrupting the iron matrix, and is heavily dominated by the alloying elements Cr, W, Mn, and V. Meanwhile the Hall-Petch contribution concerns the effect of grain size on yield stress, and the Bailey-Hirsch strengthening component [87] relates dislocation density to stress. At elevated temperatures the Hall-Petch relation breaks down, and this term is replaced by the Coble creep contribution, in cases where $\sigma_{CC} < \sigma_{HP}$ [88]. Coble creep describes the diffusion driven flow of elements along grain boundaries, and is hence a thermally activated process, only becoming stress limiting at high temperature. The dislocation strengthening contribution is itself composed of two terms which describe the effects of dislocation-dislocation interactions and dislocation-particle interactions (where particles are present). The dislocation-particle interactions are accounted for by different mechanisms at low and elevated temperature. At low temperature, dislocation strengthening is given by

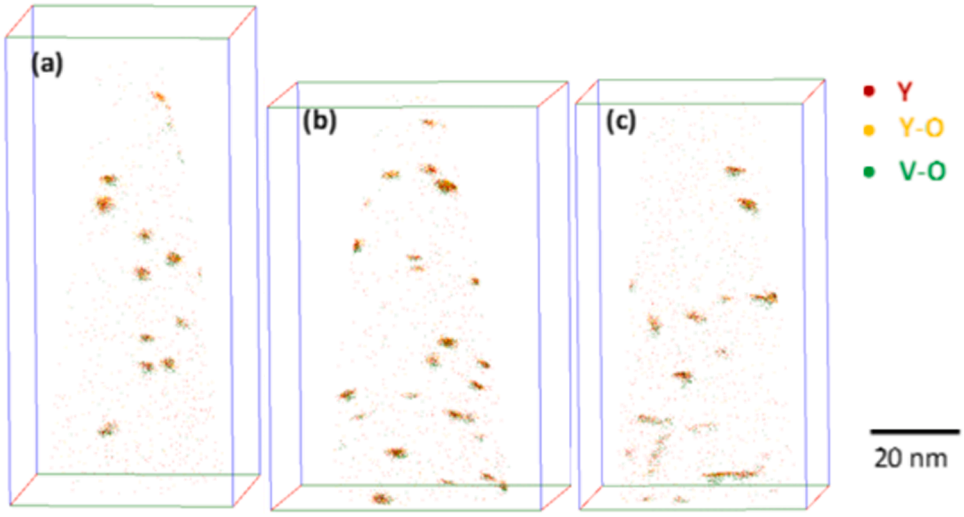

Fig. 11. Atom Probe Tomography reconstruction of Eurofer ODS steels in as-received condition (a), after tensile tests at 400 °C (b) and after tensile tests at 550 °C. The map shows only collected Y, Y-O and V-O complex ions.

$$\sigma_d = \sqrt{\sigma_{BH}^2 + \sigma_K^2} \tag{17}$$

where σ_{BH} is the dislocation-dislocation Bailey-Hirsch contribution, and σ_K is the Orowan strengthening contribution [89], which relates to dislocation bowing caused by pinning obstacles. Meanwhile at elevated temperature

$$\sigma_d = \sqrt{\sigma_{BH}^2 + \sigma_{ARW}^2} \tag{18}$$

Where $\sigma_{ARW}$is the Arzt-Rosler-Wilkinson contribution [90], which considers dislocation climb around pinning obstacles. The use of the root mean squared analysis of dislocation strengthening is utilised here, as it has been shown to more accurately model experimental yield stress in ODS steels [91–94].

All the contributions discussed are evaluated using the following set of equations (Eqs. (19), (20), and (22) [33,35,36,91,93-96], Eq. (21) [35,88,97], Eq. (23) [33,93,96,98], Eq. (24) [35,36]) such that:

$$\sigma_{SS} = 0.00689 \sum k C_i^n \tag{19}$$

$$\sigma_{HP} = \sigma_0 + \sigma_D = \sigma_0 + \left(\frac{G(T)}{G(RT)}\right)^{0.5} \cdot \frac{K_H}{\sqrt{D}} \tag{20}$$

$$\sigma_{BH} = M\theta G(T) b \rho^{0.5} \tag{21}$$

$$\sigma_{CC} = \frac{k_b T D^3 \dot{\varepsilon}}{47 \Omega \delta_B D_B} \exp(Q_B/RT) \tag{22}$$

$$\sigma_K = \frac{0.81 M G(T) b \ln\left(\frac{d\sqrt{2/3}}{|b|}\right)}{2\pi(1-\nu)^{0.5} \cdot \left(L - d\sqrt{2/3}\right)} \tag{23}$$

$$\sigma_{ARW} = 0.9M \frac{G(T) b R_T^{1.5}}{L\left(2\sqrt{2} + R_T^{1.5}\right)} \tag{24}$$

In these equations, k is an alloying element specific constant (the values for which are reported in (Table 5) [99]), C_i is the concentration in at.% of each alloying element, n is a constant, 0.75, σ_0 is the alloy's friction stress (taken as 53.9 MPa – that of single crystal Fe [92]), $G(T)$ and $G(RT)$ are the shear stress at test temperature and room temperature respectively, K_H is the Hall-Petch coefficient, D is the sample's grain size, $\dot{\varepsilon}$ is the experimental strain rate experienced by the sample, Ω is the atomic volume across the sample, δ_B is the pre-exponential factor of grain boundary diffusion, D_B is the grain boundary width, Q_B is the activation barrier energy to grain boundary diffusion, R is the gas constant (R=8.31 J/mol K), M is the Taylor factor for bcc metals, 3.06 [33,34,91,93,96,97], θ is a constant parameter, 0.33 [91,93,100-103], b is the Burgers vector modulus, ρ is the sample's dislocation density prior to yield, d is the average oxide particle size, L average particle spacing, υ is the sample's Poisson ratio, and R_T is a constant, 0.77 [35], which accounts for the loss of line tension experienced by a dislocation segment whilst pinned. The pre-exponential term moderating grain boundary diffusion, $\delta_B D_B$, is taken as 1.1 $\times 10^{-12}$ $m^3 s^{-1}$ [35,88]. The average oxide particle size was approximated as 12 nm, taken from previous TEM analysis of similarly processed ODS EUROFER97 steel [33,104]. The interparticle spacing was estimated using the equation [33,92,102,105]:

Table 5
Solid solution strengthening coefficients relating to solid solution strengthening.

Microalloying element	Strengthening coefficient, k
W	11,000
Cr	1400
Mn	7000
V	4000

$$L = d\sqrt{\frac{2}{3}}\left(\sqrt{\frac{\pi}{4f}} - 1\right) \tag{25}$$

Where f is the volume fraction, estimated as 0.0047, given the percentage by weight and relative density of Y_2O_3 within the EUROFER97 alloy. In this work the Hall-Petch coefficient was estimated through the previously used relation [35]:

$$K_H = \frac{G(RT)\sqrt{b}}{5} \tag{26}$$

Substituting this estimate into the Eq. (20) it was possible to evaluate the changing Hall-Petch contribution with temperature from the results of the XRD analysis.

The results of the constitutive flow analysis are collected in (Table 6), and shown graphically in (Fig. 12), overlaid onto which are the yield stress values found through 0.2 % offset analysis of the tensile stress-strain curves. The yield stress predicted by the constitutive flow method largely agrees well with the experimental values determined,

Table 6
Individual stress contributions to flow stress determined through Eqs. (19)-(24).

Sample	EUROFER97			ODS EUROFER97			
	RT	400 °C	550 °C	RT	400 °C	550 °C	650 °C
σ_0 [MPa]	53.9	53.9	53.9	53.9	53.9	53.9	53.9
σ_{SS} [MPa]	124.9	124.9	124.9	119.7	119.7	119.7	119.7
σ_D [MPa]	179.6	128.7	116	206.2	129.3	112.3	–
σ_{CC} [MPa]	–	–	–	–	–	–	66.2
σ_{BH} [MPa]	198.8	168.3	149.2	293.7	275.7	186.2	177.5
σ_K [MPa]	–	–	–	332.3	252.4	–	–
σ_{ARW} [MPa]	–	–	–	–	–	64.0	64.9
σ_d [MPa]	198.8	168.3	149.2	443.5	373.8	196.8	189
σ_{YS} [MPa]	557	476	444	823	677	483	429

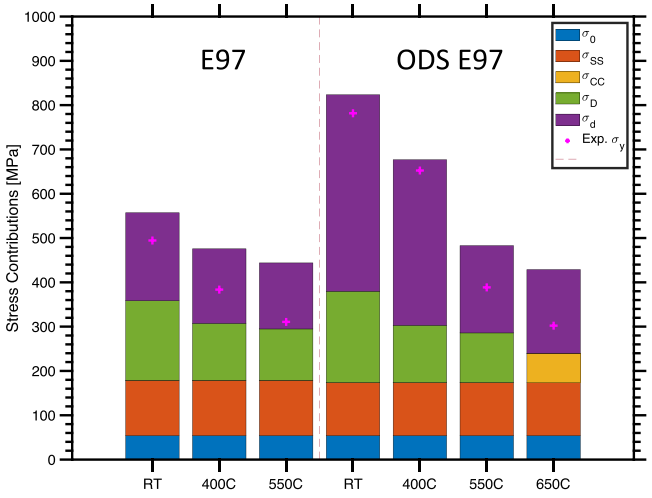

Fig. 12. Results of constitutive flow stress analysis for EUROFER97 and ODS EUROFER97 at the test temperatures considered, with the experimental yield stress recorded as a point of comparison.

the only major point of deviation being the EUROFER97 sample tested at 550 °C. Looking at the relative weight of each contribution in each instance, it is immediately apparent that the means by which dislocations move past pinning obstacles has the greatest impact on the yield strength. At room temperature and 400 °C, the dislocation strengthening dominates all other strengthening contributions but beyond 400 °C, when the Orowan bowing contribution is replaced by the weaker thermally activated Arzt-Rosler-Wilkinson contribution, the expected sharp drop in yield stress is seen.

This is borne out by the changing dislocation character, as observed in (Fig. 10). At room temperature, dislocation density is dominated by edge type dislocations, but as the test temperature is increased the screw population accounts for more of the total dislocation density, eventually dominating at 650 °C. Indeed, the transition to the screw dominated system only occurs above 400 °C: the temperature at which the Arzt-Rosler-Wilkinson contribution overcomes the Orowan bowing term. In addition, there is a sharp drop in the dislocation density plateau reached in (Fig. 9) during tensile testing between 400 °C and 550 °C, from approximately 8.5 $\times 10^{14}$ m^{-2} to 4.4 $\times 10^{14}$ m^{-2}. This similarly suggests a sudden breakdown in the pinning efficiency of the ODS particles.

The Hall-Petch relation is only observed to breakdown at 650 °C, the replacement of the Hall-Petch contribution with the lower Coble creep term accounting for the fall in yield stress observed experimentally, despite the lack of change in the dislocation density and shear moduli moving from 550 °C to 650 °C. Indeed, these results demonstrate that the drop in improved strength relative to EUROFER97 above 400 °C is almost entirely correlated to a change in the processes of deformation to thermally activated mechanisms at elevated temperatures.

Whilst the results produced in this study exhibit generally good agreement with the constitutive flow analysis predictions, it must be noted the constitutive modelling used fails to accurately predict the experimentally determined yield stress of the 550 °C EUROFER97 sample, and applying the same model to other high Cr ODS steels (Fig. 13) the accuracy of model prediction was not consistent. The results of this application are shown in (Fig. 13b) – steels with Cr content between 5wt% and 20wt% were considered, with Y_2O_3 content between 0.2wt% and 0.5wt% [19,35,91-94-98,100-103,106]. In all but one case, the constitutive flow analysis overestimated yield stress, and there are several considerations which could account for the common overestimation of yield stress seen in (Fig. 13b). Firstly, the constitutive flow analysis has a high sensitivity to several factors which are significantly challenging to accurately evaluate – the interparticle spacing, particle size, and dislocation density. Such evaluation relies either on snapshots of material microstructure offered through TEM to calculate average values or larger interaction volume informed microstructural characterisation, as employed here, the first of which offers precise measurement which may represent local area rather than across sample properties, the second of which may produce more representative results at the expense of precision. Secondly, there is disagreement across existing literature as to appropriate values of utilised constants: the Taylor Factor, M, is reported between 2.5 [103] and 3.1 [88,94] for bcc metals, the frictional stress, σ_0, is most commonly reported as 53.9 MPa, but has been reported between 100 MPa [88] and 13 MPa [35,36], and the parameter θ is reported between 0.2 [94] and 0.5 [19,107]. Beyond this, there are significant assumptions introduced in the evaluation of every term:

1. The use of a single, stable value for the matrix frictional stress, σ_0, independent of temperature
2. That all microalloying elemental content will contribute to solid solution strengthening, disregarding the proclivity of elements such as Cr and W to form precipitates within ODS steels.
3. Similarly, that the entire dislocation density population recorded will contribute to dislocation forest strengthening

Despite these limitations, the current work demonstrates that constitutive flow analysis can provide accurate assessment of material flow stress, and allows changes in flow stress to be described in microstructural terms. Assessment of microstructural contributions to flow stress in this work and the literature referenced informs future refinement of next generation fusion materials – identifying key parameters for the optimisation of oxide dispersion strengthening. Microstructural phenomena can be expected to fundamentally control macroscopic performance, and work directly connecting the two provides necessary insight into how fabrication and processing can be controlled to optimise performance criteria. The results presented here emphasize both the degree to which introduction and control of appropriate precipitates can positively augment material properties, and the increased importance of dislocation behaviour with the introduction of ODS; the temperature at which edge and screw dislocations become comparable corresponding to a significant decrease in yield stress. Within the context of existing literature, these results help to build up a more complete picture of the ODS design space. The design and production of new structural materials, able to withstand higher operating temperature, will have important consequences for fusion reactor design; increased operating temperature allows for increased coolant cycle temperature, leading to increased efficiency of reactor energy production. Considering the proposed lifetime of currently considered nuclear fusion reactors, even small increases in efficiency can be expected to yield significant rewards, and optimisation of every aspect of reactor design is the best path to viable fusion energy.

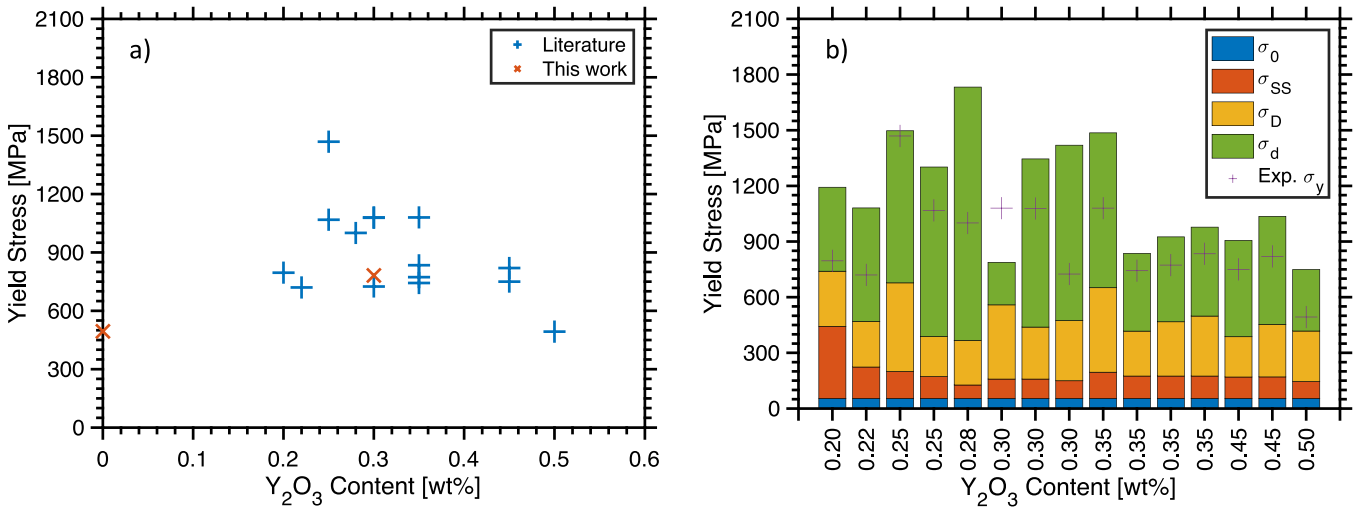

Fig. 13. a) Figure demonstrating effect of Y_2O_3 content on yield stress in high Cr ODS steels, b) comparative constitutive flow analysis of different wt% Y_2O_3 ODS steels demonstrating suitability and limitations of the constitutive flow model employed. The data presented is taken (left to right in subfigure b)) from Zhao et al. (2022), Chauhan et al. (2017), Kim et al. (2012), Shen et al. (2016), Cunningham et al. (2014), De Sanctis et al. (2018), Praud et al. (2013), Cao et al. (2021), Jarugula et al. (2021), Ren et al. (2018), Ren et al. (2018), Ren et al. (2018), Li et al. (2019), Li et al. (2019), and Wang et al. (2013). Contributing data is summarized in Supplementary Table 1.

4. Conclusion

The elastic and mechanical properties of the promising reduced activation ferritic/martensitic steel EUROFER97, and an oxide-dispersion strengthened variant of this alloy were established using in-situ high energy X-ray diffraction during tensile testing. The strengthening effect of ODS particles was noted at room temperature, though this effect lessened with elevated temperatures, as oxide particles became less significant pinning obstacles. The single crystal elastic constants of EUROFER97 and ODS EUROFER97 at RT were determined in GPa as $C_{11} = 230 \pm 10$, $C_{12} = 130 \pm 10$, $C_{44} = 119 \pm 1$ and $C_{11} = 243 \pm 5$, $C_{12} = 136 \pm 6$, $C_{44} = 114.0 \pm 0.6$ respectively. Further the dislocation density of the test samples during deformation were evaluated through the modified Williamson-Hall method, and in addition to the increased annihilation imparted by elevated temperature, and the presence of ODS particles promoting dislocation formation, it was found that dislocation character became almost purely screw at elevated temperature. Using the material properties determined through XRD analysis, the yield strength of both materials at room temperature was approximated using constitutive flow modelling, revealing the relative influence of strengthening contribution in each case – Orowan bowing of dislocations around pinning obstacles in particular accounting for the ODS material's enhanced strength up to 400 °C, and the advent of thermally activated dislocation climb and grain boundary diffusion producing the sharp declination in strength experienced above 400 °C.

Declaration of competing interest

The authors declare that they have no known competing financial interests or personal relationships that could have appeared to influence the work reported in this paper.

Acknowledgements

We give thanks to the Karlsruhe Institute for Technology for providing the EUROFER97 and ODS EUROFER97 materials for this study. Funding for this work was provided by the United Kingdom Atomic Energy Authority (UKAEA) and the School of Metallurgy & Materials at University of Birmingham,. We acknowledge the Diamond Light Source for beamtime on the I12 beamline under proposal (EE19251). The authors thank the University of Manchester at Harwell for access to the ETMT for beamline use. Dr Cai thanks for the funding support from the UKRI Future Leaders Fellowship (MR/W007967/1). Dr Wang, Dr Kuksenko, and Dr Gorley would like to acknowledge the EPSRC grants (EP/T012250/1 and EP/W006839/1) and the Department for Energy Security and Net Zero.

Supplementary materials

Supplementary material associated with this article can be found, in the online version, at doi:10.1016/j.actamat.2024.119876.

References

[1] A. Möslang, et al., Towards reduced activation structural materials data for fusion DEMO reactors, Nucl. Fusion 45 (7) (2005) 649–655.
[2] A.A.F. Tavassoli, E. Diegele, R. Lindau, N. Luzginova, H. Tanigawa, Current status and recent research achievements in ferritic/martensitic steels, J. Nucl. Mater. 455 (1–3) (2014) 269–276.
[3] H. Tanigawa, K. Shiba, H. Sakasegawa, T. Hirose, S. Jitsukawa, Technical issues related to the development of reduced-activation ferritic/martensitic steels as structural materials for a fusion blanket system, Fusion Eng. Des. 86 (9–11) (2011) 2549–2552.
[4] M. Zmitko, et al., The European ITER Test Blanket Modules: EUROFER97 material and TBM's fabrication technologies development and qualification, Fusion Eng. Des. 124 (2017) 767–773.
[5] L.V. Boccaccini, et al., Objectives and status of EUROfusion DEMO blanket studies, Fusion Eng. Des. 109–111 (2016) 1199–1206.
[6] L. Forest, et al., Status of the EU DEMO breeding blanket manufacturing R&D activities, Fusion Eng. Des. 152 (October 2018) (2020) 111420.
[7] F. Tavassoli, Eurofer steel, development to full code qualification, Procedia Eng 55 (2013) 300–308.
[8] K.D. Zilnyk, K.G. Pradeep, P. Choi, H.R.Z. Sandim, D. Raabe, Long-term thermal stability of nanoclusters in ODS-Eurofer steel: an atom probe tomography study, J. Nucl. Mater. 492 (2017) 142–147.
[9] L. Tan, L.L. Snead, Y. Katoh, Development of new generation reduced activation ferritic-martensitic steels for advanced fusion reactors, J. Nucl. Mater. 478 (2016) 42–49.
[10] L. Tan, Y. Katoh, L.L. Snead, Development of castable nanostructured alloys as a new generation RAFM steels, J. Nucl. Mater. 511 (2018) 598–604.
[11] G. Yu, N. Nita, N. Baluc, Thermal creep behaviour of the EUROFER 97 RAFM steel and two European ODS EUROFER 97 steels, Fusion Eng. Des. 75–79 (SUPPL) (2005) 1037–1041.
[12] P. Fernandez, A.M. Lancha, J. Lapena, D. Gomez-Briceno, M. Serrano, M. Hernandez-Mayoral, Reduced activation Ferritic/Martensitic Steel Eurofer'97 as possible structural material for fusion Devices. Metallurgical characterization on as-received condition and after simulated service conditions, Inf. Técnicos Ciemat (2004) 73.
[13] P. Fernández, A.M. Lancha, J. Lapeña, M. Hernández-Mayoral, Metallurgical characterization of the reduced activation ferritic/martensitic steel Eurofer'97 on as-received condition, Fusion Eng. Des. 58–59 (2001) 787–792.

[14] M. Klimenkov, R. Lindau, E. Materna-Morris, A. Möslang, TEM characterization of precipitates in EUROFER 97, Prog. Nucl. Energy 57 (2012) 8–13.
[15] S.J. Zinkle, et al., Development of next generation tempered and ODS reduced activation Ferritic/martensitic steels for fusion energy applications, Nucl. Fusion 57 (9) (2017).
[16] R. Andreani, M. Gasparotto, Overview of fusion nuclear technology in Europe, Fusion Eng. Des. 61–62 (2002) (2002) 27–36.
[17] R. Lindau, et al., Present development status of EUROFER and ODS-EUROFER for application in blanket concepts, Fusion Eng. Des. 75–79 (SUPPL) (2005) 989–996.
[18] A. Wasilkowska, M. Bartsch, U. Messerschmidt, R. Herzog, A. Czyrska-Filemonowicz, Creep mechanisms of ferritic oxide dispersion strengthened alloys, J. Mater. Process. Technol. 133 (1–2) (2003) 218–224.
[19] J. Wang, W. Yuan, R.S. Mishra, I. Charit, Microstructure and mechanical properties of friction stir welded oxide dispersion strengthened alloy, J. Nucl. Mater. 432 (1–3) (2013) 274–280.
[20] P. Olier, A. Bougault, A. Alamo, Y. de Carlan, Effects of the forming processes and Y2O3 content on ODS-Eurofer mechanical properties, J. Nucl. Mater. 386–388 (C) (2009) 561–563.
[21] Y. de Carlan, et al., CEA developments of new ferritic ODS alloys for nuclear applications, J. Nucl. Mater. 386–388 (C) (2009) 430–432.
[22] D. Kumar, U. Prakash, V.V. Dabhade, K. Laha, T. Sakthivel, High yttria ferritic ODS steels through powder forging, J. Nucl. Mater. 488 (2017) 75–82.
[23] Z. Lu, R.G. Faulkner, N. Riddle, F.D. Martino, K. Yang, Effect of heat treatment on microstructure and hardness of Eurofer 97, Eurofer ODS and T92 steels, J. Nucl. Mater. 386–388 (C) (2009) 445–448.
[24] A. Alamo, H. Regle, G. Pons, J.L. Béchade, Microstructure and textures of Ods ferritic alloys obtained by mechanical alloying, Mater. Sci. Forum 88–90 (January) (1992) 183–190.
[25] J. Shen, et al., Study on anisotropy in microstructure and tensile properties of the 12Cr oxide dispersion strengthened (ODS) steel, Fusion Eng. Des. 146 (February) (2019) 1082–1085.
[26] R. Blondé, et al., High-energy X-ray diffraction study on the temperature-dependent mechanical stability of retained austenite in low-alloyed TRIP steels, Acta Mater 60 (2) (2012) 565–577.
[27] X. Zhang, et al., In situ high-energy X-ray diffraction study of tensile deformation of neutron-irradiated polycrystalline Fe-9%Cr alloy, Acta Mater 126 (2017) 67–76.
[28] R.A. Renzetti, H.R.Z. Sandim, R.E. Bolmaro, P.A. Suzuki, A. Möslang, X-ray evaluation of dislocation density in ODS-Eurofer steel, Mater. Sci. Eng. A 534 (2012) 142–146.
[29] G.M. Stoica, A.D. Stoica, M.K. Miller, D. Ma, Temperature-dependent elastic anisotropy and mesoscale deformation in a nanostructured ferritic alloy, Nat. Commun. 5 (2014) 1–8.
[30] J.L. Lin, et al., In situ synchrotron tensile investigations on 14YWT, MA957, and 9-Cr ODS alloys, J. Nucl. Mater. 471 (2016) 289–298.
[31] Y. Gan, et al., Temperature effect of elastic anisotropy and internal strain development in advanced nanostructured alloys: an in-situ synchrotron X-ray investigation, Mater. Sci. Eng. A 692 (March) (2017) 53–61.
[32] K. Mo, et al., Synchrotron study on load partitioning between ferrite/martensite and nanoparticles of a 9Cr ODS steel, J. Nucl. Mater. 455 (1–3) (2014) 376–381.
[33] J. Fu, J.C. Brouwer, R.W.A. Hendrikx, I.M. Richardson, M.J.M. Hermans, Microstructure characterisation and mechanical properties of ODS Eurofer steel subject to designed heat treatments, Mater. Sci. Eng. A 770 (2020).
[34] R. Husák, H. Hadraba, Z. Chlup, M. Heczko, T. Kruml, V. Puchý, ODS EUROFER steel strengthened by y-(Ce, hf, la, sc, and zr) complex oxides, Metals (Basel) 9 (11) (2019) 1–14.
[35] M. De Sanctis, et al., Temperature dependent mechanical behavior of ods steels, Mater. Sci. Forum 941 MSF (2018) 257–262.
[36] M. De Sanctis, et al., Mechanical characterization of a nano-ODS steel prepared by low-energy mechanical alloying, Metals (Basel) 7 (8) (2017) 1–12.
[37] Y.Q. Wang, M. Gorley, S. Kabra, E. Surrey, Influence of a 1.5 T magnetic field on the tensile properties of Eurofer-97 steel, Fusion Eng. Des. 141 (January) (2019) 68–72.
[38] R.A. Renzetti, H.R.Z. Sandim, A.F. Padilha, D. Raabe, R. Lindau, A. Möslang, Annealing effects on the microstructure of ferritic-martensitic ODS-Eurofer steel, Fusion Sci. Technol. 60 (1 T) (2011) 22–26.
[39] F. Bachmann, R. Hielscher, H. Schaeben, Grain detection from 2d and 3d EBSD data-Specification of the MTEX algorithm, Ultramicroscopy 111 (12) (2011) 1720–1733.
[40] F. Bachmann, R. Hielscher, H. Schaeben, Texture analysis with MTEX- Free and open source software toolbox, Solid State Phenom 160 (2010) 63–68.
[41] B. Gault, M. Moody, J. Cairney, S. Ringer, Atom Probe Microscopy, Springer Series in Materials Science, 2012.
[42] M. Miller, Atom Probe Tomography: Analysis at the Atomic Level, Kluwer Academic/Plenum Publishers, New York, 2000.
[43] M. Drakopoulos, et al., I12: the Joint Engineering, Environment and Processing (JEEP) beamline at Diamond Light Source, J. Synchrotron Radiat. 22 (2015) (2015) 828–838.
[44] J. Filik, et al., Processing two-dimensional X-ray diffraction and small-angle scattering data in DAWN 2, J. Appl. Crystallogr. 50 (3) (2017) 959–966.
[45] M. Basham, et al., Data Analysis WorkbeNch (DAWN), J. Synchrotron Radiat. 22 (2015) 853–858.
[46] M.L. Hart, M. Drakopoulos, C. Reinhard, T. Connolley, Complete elliptical ring geometry provides energy and instrument calibration for synchrotron-based two-dimensional X-ray diffraction, J. Appl. Crystallogr. 46 (5) (2013) 1249–1260.
[47] A. Borbély, J. Dragomir-Cernatescu, G. Ribárik, T. Ungár, Computer program ANIZC for the calculation of diffraction contrast factors of dislocations in elastically anisotropic cubic, hexagonal and trigonal crystals, J. Appl. Crystallogr. 36 (1) (2003) 160–162.
[48] R. De Wit, Diffraction elastic constants of a cubic polycrystal, J. Appl. Crystallogr. 30 (4) (1997) 510–511.
[49] T. Ungár, I. Dragomir, Á. Révész, A. Borbély, The contrast factors of dislocations in cubic crystals: the dislocation model of strain anisotropy in practice, J. Appl. Crystallogr. 32 (5) (1999) 992–1002.
[50] T. Ungár, A. Borbély, The effect of dislocation contrast on x-ray line broadening: a new approach to line profile analysis, Appl. Phys. Lett. 69 (21) (1996) 3173–3175.
[51] D.A. McClintock, M.A. Sokolov, D.T. Hoelzer, R.K. Nanstad, Mechanical properties of irradiated ODS-EUROFER and nanocluster strengthened 14YWT, J. Nucl. Mater. 392 (2) (2009) 353–359.
[52] E. Brochen, J. Pötschke, C.G. Aneziris, Improved thermal stress resistance parameters considering temperature gradients for bricks in refractory linings, Int. J. Appl. Ceram. Technol. 11 (2) (2014) 371–383.
[53] R.W. Conn, First wall and divertor plate material selection in fusion reactors, J. Nucl. Mater. 76–77 (C) (1978) 103–111.
[54] A. Paúl, A. Beirante, N. Franco, E. Alves, J.A. Odriozola, Phase transformation and structural studies of EUROFER RAFM alloy, Mater. Sci. Forum 514–516 (PART 1) (2006) 500–504.
[55] P. Norajitra, 3 - Detailed Design of a Helium cooled Divertor for a Fusion Power Plant. Divertor Development for a Future Fusion Power Plant, KIT Scientific Publishing, 2011, pp. 29–104.
[56] K.W. Katahara, M.H. Manghnani, E.S. Fisher, Pressure derivatives of the elastic moduli of BCC Ti-V-Cr, Nb-Mo and Ta-W alloys, J. Phys. F Met. Phys. 9 (5) (1979) 773–790.
[57] J.D. Greiner, O.N. Carlson, J.F. Smith, Single-crystal elastic constants of vanadium and vanadium with oxygen additions, J. Appl. Phys. 50 (6) (1979) 4394–4398.
[58] J.A. Rayne, B.S. Chandrasekhar, Elastic constants of iron from 4.2 to 300°K, Phys. Rev. 122 (6) (1961) 1714–1716.
[59] S.A. Kim, W.L. Johnson, Elastic constants and internal friction of martensitic steel, ferritic-pearlitic steel, and α-iron, Mater. Sci. Eng. A 452–453 (2007) 633–639.
[60] P. Magaud, F. Le Vagueres, Annual report of the annual report of the association CEA /EURATOM, Fusion Technol (1996).
[61] V.I. Razumovskiy, A.V. Ruban, P.A. Korzhavyi, Effect of temperature on the elastic anisotropy of pure Fe and Fe 0.9Cr0.1 random alloy, Phys. Rev. Lett. 107 (20) (2011) 1–5.
[62] F. Tavassoli, "Fusion demo interim structural design criteria (DISDC) Appendix A material design limit data," 2004.
[63] K. Mergia, N. Boukos, Structural, thermal, electrical and magnetic properties of Eurofer 97 steel, J. Nucl. Mater. 373 (1–3) (2008) 1–8.
[64] G. Zhang, et al., The evolution of internal stress and dislocation during tensile deformation in a 9Cr ferritic/martensitic (F/M) ODS steel investigated by high-energy X-rays, J. Nucl. Mater. 467 (2015) 50–57.
[65] M. Li, L. Wang, J.D. Almer, Dislocation evolution during tensile deformation in ferritic-martensitic steels revealed by high-energy X-rays, Acta Mater 76 (2014) 381–393.
[66] Q. Tian, et al., Study of micro-plastic deformation in pure iron before macro-yielding using acoustic emission, electron backscattered diffraction and transmission electron microscopy, Mater. Sci. Eng. A 771 (July 2019) (2020) 138645.
[67] W.D. Brentnall, W. Rostoker, Some observations on microyielding, Acta Metall 13 (3) (1965) 187–198.
[68] S. Takaki, D. Akama, N. Nakada, T. Tsuchiyama, Effect of grain boundary segregation of interstitial elements on hallpetch coefficient in steels, Mater. Trans. 55 (1) (2014) 28–34.
[69] F. Mompiou, M. Legros, D. Caillard, H. Mughrabi, In situ TEM observations of reverse dislocation motion upon unloading of tensile-deformed UFG aluminium, J. Phys. Conf. Ser. 240 (2010).
[70] H. Adachi, H. Mizowaki, M. Hirata, D. Okai, H. Nakanishi, Measurement of dislocation density change during tensile deformation in coarse-grained aluminum by in-situ XRD technique with tester oscillation+1, Mater. Trans. 62 (1) (2021) 62–68.
[71] H. Adachi, Y. Miyajima, M. Sato, N. Tsuji, Evaluation of dislocation density for 1100 aluminum with different grain size during tensile deformation by using In-situ X-ray diffraction technique, Keikinzoku/J. Japan Inst. Light Met. 64 (10) (2014) 463–469.
[72] H. Adachi, Y. Karamatsu, S. Nakayama, T. Miyazawa, M. Sato, T. Yamasaki, Elastic and plastic deformation behavior studied by in-situ synchrotron x-ray diffraction in nanocrystalline nickel, Mater. Trans. 57 (9) (2016) 1447–1453.
[73] S. Takaki, T. Masumura, T. Tsuchiyama, Dislocation characterization by the direct-fitting/modified Williamson–Hall (DF/mWH) method in cold worked ferritic steel, ISIJ Int 59 (3) (2019) 567–572.
[74] D. Hull, D.J. Bacon, Movement of Dislocations. Introduction to Dislocations, Elsevier Ltd, 2011, pp. 43–62.
[75] Y.H. Zhang, E. Ma, J. Sun, W.Z. Han, A unified model for ductile-to-brittle transition in body-centered cubic metals, J. Mater. Sci. Technol. 141 (2023) 193–198.
[76] Y. Lu, Y.H. Zhang, E. Ma, W.Z. Han, Relative mobility of screw versus edge dislocations controls the ductile-to-brittle transition in metals, Proc. Natl. Acad. Sci. U. S. A. 118 (37) (2021) 1–6.

[77] Y.H. Zhang, W.Z. Han, Mechanism of brittle-to-ductile transition in tungsten under small-punch testing, Acta Mater 220 (2021) 117332.
[78] C. Lee, et al., Strength can be controlled by edge dislocations in refractory high-entropy alloys, Nat. Commun. 12 (1) (2021) 6–13.
[79] C. Baruffi, F. Maresca, W.A. Curtin, Screw vs. edge dislocation strengthening in body-centered-cubic high entropy alloys and implications for guided alloy design, MRS Commun 12 (6) (2022) 1111–1118.
[80] G. Bonny, D. Terentyev, L. Malerba, Interaction of screw and edge dislocations with chromium precipitates in ferritic iron: an atomistic study, J. Nucl. Mater. 416 (1–2) (2011) 70–74.
[81] G. Monnet, S. Naamane, B. Devincre, Orowan strengthening at low temperatures in bcc materials studied by dislocation dynamics simulations, Acta Mater 59 (2) (2011) 451–461.
[82] R. Lesar, Simulations of dislocation structure and response, Annu. Rev. Condens. Matter Phys. 5 (1) (2014) 375–407.
[83] C.A. Williams, E.A. Marquis, A. Cerezo, G.D.W. Smith, Nanoscale characterisation of ODS-Eurofer 97 steel: an atom-probe tomography study, J. Nucl. Mater. 400 (1) (2010) 37–45.
[84] E.O. Hall, The deformation and ageing of mild steel: III Discussion of results, Proc. Phys. Soc. Sect. B 64 (9) (1951) 747–753.
[85] A. Cracknell, N.J. Petch, Frictional forces on dislocation arrays at the lower yield point in iron, Acta Metall 3 (2) (1955) 186–189.
[86] R.L. Coble, A model for boundary diffusion controlled creep in polycrystalline materials, J. Appl. Phys. 34 (6) (1963) 1679–1682.
[87] J.E. Bailey, P.B. Hirsch, The dislocation distribution, flow stress, and stored energy in cold-worked polycrystalline silver, Philos. Mag. 5 (53) (1960) 485–497.
[88] S. Seils, A. Kauffmann, F. Hinrichs, D. Schliephake, T. Boll, M. Heilmaier, Temperature dependent strengthening contributions in austenitic and ferritic ODS steels, Mater. Sci. Eng. A 786 (January) (2020) 139452.
[89] E. Orowan, Symposium on Internal Stresses in Metals and Alloys, Institute of Metal, London, 1948.
[90] J. Rösler, E. Arzt, A new model-based creep equation for dispersion strengthened materials, Acta Metall. Mater. 38 (4) (1990) 671–683.
[91] A. Chauhan, et al., Microstructure characterization and strengthening mechanisms of oxide dispersion strengthened (ODS) Fe-9 %Cr and Fe-14 %Cr extruded bars, J. Nucl. Mater. 495 (2017) 6–19.
[92] J. Shen, et al., Microstructural characterization and strengthening mechanisms of a 12Cr-ODS steel, Mater. Sci. Eng. A 673 (2016) 624–632.
[93] R. Jarugula, S. Channagiri, S.G.S. Raman, G. Sundararajan, Strengthening mechanisms in nano oxide dispersion-strengthened Fe-18Cr ferritic steel at different temperatures, Metall. Mater. Trans. A Phys. Metall. Mater. Sci. 52 (5) (2021) 1901–1912.
[94] R. Zhao, H. Jia, S. Cao, Z. Tong, Z. Zhou, Effect of the addition of Y and Y2O3 on microstructure and mechanical properties of 15Cr-15Ni ODS steel, Nucl. Mater. Energy 31 (May) (2022) 101196.
[95] Y. Li, L. Zhang, D. Long, L. Yu, H. Li, The precipitated particle refinement in high-cr ods steels by microalloying element addition, Materials (Basel) 14 (24) (2021) 1–12.
[96] S. Xu, Z. Zhou, H. Jia, Z. Yao, Microstructure characterization and mechanical properties of Al alloyed 9Cr ODS steels with different Al contents, Steel Res. Int. 90 (7) (2019) 1–11.
[97] J.H. Schneibel, M. Heilmaier, Hall-petch breakdown at elevated temperatures, Mater. Trans. 55 (1) (2015) 44–51.
[98] J.H. Kim, T.S. Byun, D.T. Hoelzer, C.H. Park, J.T. Yeom, J.K. Hong, Temperature dependence of strengthening mechanisms in the nanostructured ferritic alloy 14YWT: part II-Mechanistic models and predictions, Mater. Sci. Eng. A 559 (2013) 111–118.
[99] Q. Li, Modeling the microstructure-mechanical property relationship for a 12Cr-2W-V-Mo-Ni power plant steel, Mater. Sci. Eng. A 361 (1–2) (2003) 385–391.
[100] W. Li, H. Xu, X. Sha, J. Meng, Z. Wang, Microstructure and mechanical properties of 14Cr-ODS steels with Zr addition, High Temp. Mater. Process 38 (2019) (2019) 404–410.
[101] J. Ren, L. Yu, Y. Liu, C. Liu, H. Li, J. Wu, Effects of Zr addition on strengthening mechanisms of al-alloyed high-Cr ODS steels, Materials (Basel) 11 (1) (2018) 1–13.
[102] S. Cao, Z. Zhou, Microstructure and mechanical properties of an ODS ferritic steel with very low Cr content, J. Nucl. Mater. 551 (2021) 152971.
[103] M. Praud, et al., Study of the deformation mechanisms in a Fe-14 % Cr ODS alloy, J. Nucl. Mater. 428 (1–3) (2012) 90–97.
[104] M. Klimiankou, R. Lindau, A. Möslang, HRTEM study of yttrium oxide particles in ODS steels for fusion reactor application, J. Cryst. Growth 249 (1–2) (2003) 381–387.
[105] B. Kombaiah, K.L. Murty, Coble, Orowan strengthening, and dislocation climb mechanisms in a Nb-Modified Zircaloy cladding, Metall. Mater. Trans. A Phys. Metall. Mater. Sci. 46 (10) (2015) 4646–4660.
[106] N. Cunningham, Y. Wu, D. Klingensmith, G.R. Odette, On the remarkable thermal stability of nanostructured ferritic alloys, Mater. Sci. Eng. A 613 (2014) 296–305.
[107] A. Steckmeyer, et al., Tensile properties and deformation mechanisms of a 14Cr ODS ferritic steel, J. Nucl. Mater. 405 (2) (2010) 95–100.